scientific reports

Check for updates

OPEN

Nonlinear dynamics of a non-stationary rotor-disk-bearing system with rub-impact and geometric nonlinearity under non-ideal excitation

Mohammad Amin Ghasemi[1], Saeed Bab[2] & Morteza Karamooz Mahdiabadi[1]✉

This study investigates the nonlinear dynamic behavior of a non-stationary rotor-disk-bearing system subjected to rub-impact phenomena under varying operational conditions. The rotor is modeled as an Euler–Bernoulli beam, with rigid-body disks and bearings represented using both linear and nonlinear spring elements to accurately capture dynamic characteristics. The model incorporates inherent system nonlinearities, including large deflections, non-ideal external excitations, and rub-impact forces consisting of normal contact and frictional components. Rub-impact is triggered when the rotor's vibrational amplitude exceeds the radial clearance, activating contact interactions with the stator. The governing equations of motion are derived and solved using both numerical simulations and the analytical averaging method, demonstrating strong agreement. Results show that rub-impact significantly alters the system's vibrational response, particularly near critical speeds, leading to amplitude amplification, prolonged resonance, energy localization, and the emergence of the Sommerfeld effect. Parametric studies further evaluate the effects of damping, nonlinear bearing stiffness, and variations in applied torque on system behavior.

Keywords Rotor-disk-bearing, Non-stationary analysis, Rub-impact, Elastic supports, Non-ideal energy source

Rotating systems are widely used in various industries. Turbomachinery is employed to extract or perform work on fluids. These machines typically consist of rotating and stationary components, with the rotating part referred to as the rotor. With the advancement of industry and the increase in rotational speeds of machines, studying the dynamic behavior of these systems has gained significant importance. Developing an appropriate physical model of the real system is essential for examining the dynamic behavior of a rotating system. The first theoretical model in rotor dynamics is the Jeffcott model, which consists of a flexible, massless shaft with a disk placed at its center[1].

In general, rotating systems are simulated under various conditions to analyze the impact of parameter changes and different configurations in the model geometry, facilitating the study of their dynamic behavior. The nonlinear dynamics and stability of rotor-bearing systems under different conditions have been extensively studied. Phadatare and Pratiher[2] examined the chaotic behaviors and nonlinear responses of a rotor-disk-bearing system with geometric eccentricity and mass unbalance, highlighting complex dynamics through a large deflection model. In a complementary study, they analyzed the dynamic stability and bifurcation phenomena in axially loaded flexible shaft-disk systems, focusing on flexible bearing support[3]. Moradi Tiaki et al.[4] investigated the influence of gravity on the nonlinear free vibrations of overhung rotors, emphasizing significant geometric effects. Ali Nezhad et al.[5] presented a comprehensive analysis of coupled flexural-extensional-torsional vibrations in composite spinning shafts, incorporating geometrical nonlinearity.

The nonlinear dynamics of rotor-bearing systems have been extensively studied with a focus on bearing characteristics influencing vibration and stability. Jain and Bhosle[6] modeled nonlinear vibrations in ball bearings

[1]Department of Mechanical Engineering, Tarbiat Modares University, P.O. Box 14115-177 Tehran, Iran. [2]Mechanical Rotary Equipment Department, Niroo Research Institute, Dadman street, P.O. Box 14665-517 Tehran, Iran. ✉email: karamooz@modares.ac.ir

due to radial clearance and the number of balls, offering insights into system response. Liang et al.[7] studied how rolling bearing parameters impact the nonlinear dynamics of offset rotors. Zhou et al.[8] analyzed rotor systems supported by ball bearings with floating-ring squeeze film dampers, revealing complex dynamic responses. Al-Solihat and Behdinan[9] investigated the force transmissibility and frequency response of flexible shaft-disk rotors in nonlinear suspension systems. Jin et al.[10] proposed a nonlinear force model to replace the traditional Hertzian contact model in rigid-rotor ball bearing systems. Zhang et al.[11,12] addressed time-varying bearing stiffness and looseness effects on rotor systems. Bai et al.[13] studied subharmonic resonance in symmetric ball bearing-rotor systems, while Yang et al.[14] focused on super-harmonic resonance caused by local defects in the outer raceway. Moreover, the nonlinear response of rotor systems with bearing dynamic misalignment has been extensively studied, revealing significant nonlinearities that affect stability, vibration, and resonance characteristics. Advanced models incorporating misalignment, such as those in[15], have provided valuable insights into real-world behaviors and strategies for optimizing design and maintenance. These studies collectively advance the understanding of nonlinear interactions and instabilities in rotor dynamics. Multi-rotor systems and reinforced structures have attracted significant attention due to their complex dynamics and practical applications. Recent advancements highlight the role of innovative materials, structural flexibility, and fault-tolerant designs in improving system performance. For instance, graphene nanoplatelet-reinforced rotors[16] have demonstrated enhanced vibration resistance. Moreover, a nonlinear energy sink in a rotating system with journal bearings can significantly reduce the vibration amplitudes[17]. While the incorporation of disk flexibility has revealed its critical influence on nonlinear dynamic behavior[18]. Temperature variations and material properties in ceramic bearings further underscore the importance of environmental factors in stability analysis[19]. Moreover, advanced damping mechanisms such as acoustic black holes have emerged as effective solutions for vibration attenuation, offering innovative approaches to dynamic control[20,21]. In dual-rotor systems, the interaction of faults like looseness and rub-impact with nonlinear features, including elastic supports and friction dampers, has provided deeper insights into fault dynamics and system resilience[22,23].Collectively, these findings contribute to a more comprehensive understanding of the challenges and opportunities in designing robust multi-rotor systems.

Rub-impact phenomena in rotor systems, particularly in high-speed rotating machinery such as aero-engines, are critical due to their substantial impact on system performance, longevity, and safety. The interaction between rotor and stator components, such as the rubbing of blades against casings or other parts, introduces significant nonlinearities into the system dynamics. Understanding these nonlinear interactions is essential for predicting failures and optimizing system design. Studies have shown that rub-impact can lead to unstable vibrations, nonlinear modal interactions, and, in extreme cases, catastrophic failure if not properly managed. The importance of analyzing flexible and rigid blades, rotor-bearing interactions, and the effects of mass unbalance on vibration characteristics has been well-established[24,25]. Furthermore, the incorporation of nonlinear supports and the complexities introduced by blade interconnections add further challenges to understanding the dynamic behavior of rotor systems[26,27]. In addition to this, advanced methods for monitoring blade damage through vibration analysis have proven invaluable in maintaining rotor system integrity, allowing for early detection of potential issues before they lead to failure[28]. Overall, these studies highlight the importance of rub-impact analysis in rotor dynamics, offering vital insights into the nonlinear stability and vibrational behavior of such systems[29–31].

The analysis of non-stationary dynamics is crucial for understanding the behavior of mechanical systems, especially in rotating machinery. Unlike stationary systems with constant parameters, non-stationary systems exhibit time-varying forces, motions, and vibrations, making their behavior more complex. Investigating such systems is essential for accurately predicting performance under real-world conditions, where transient phenomena, speed fluctuations, and external disturbances are common. This analysis is vital for ensuring the stability, reliability, and longevity of systems exposed to fluctuating operational environments.the dynamic behavior of nonlinear rotating shafts and rotor systems under non-stationary conditions has been extensively studied due to its impact on the stability and reliability of mechanical systems. Mahmoudi et al.[32,33] explored the non-stationary dynamics of shafts passing through critical speeds, highlighting the effects of geometrical nonlinearity and excitation from non-ideal energy sources. Similarly, Kafi and Hosseini[34] investigated the dynamics of nonlinear composite shafts subjected to non-ideal energy sources, providing valuable insights into vibration reduction strategies. Other studies, such as those by Bab et al.[35] and Iskakov and Jamalov[36], addressed the mitigation of non-stationary vibrations in rotor systems through methods like nonlinear absorbers and resonance control techniques. Recent advancements in this field include the work by Rokn-abadi and Amirzadegan[37], who focused on rotor misalignment, and Sghaier et al.[38], who studied coupled bending-torsional vibrations of rotors under complex non-stationary operating conditions.

In this paper, the dynamic behavior of a rotor-disk-bearing system is investigated and analyzed under non-stationary operational conditions, considering the effects of rub-impact and nonlinear bearing stiffness.The equations of motion are derived by extracting the kinetic and potential energies of the system components and subsequently applying Hamilton's principle. The analysis incorporates rotary inertia and gyroscopic effects based on Euler-Bernoulli beam theory. The contact between the disks and the stator is elastically modeled using Coulomb frictional forces moreover, the excitation motor is considered non-ideal, with the applied torque decreasing as rotational speed increases, following a coefficient specific to the motor's characteristics[39]. After deriving the equations of motion, they are solved using the averaging method.The accuracy of the results is validated through comparisons with numerical solutions obtained via the Runge–Kutta method.The dynamic behavior of the system during the passage through critical speeds is analyzed using time-domain amplitude diagrams for various torques, damping coefficients, nonlinear coefficients, and unbalance parameters. Additionally, the likelihood of Sommerfeld effect occurrence and the system's inability to transition through critical speeds under different operating conditions are thoroughly examined.

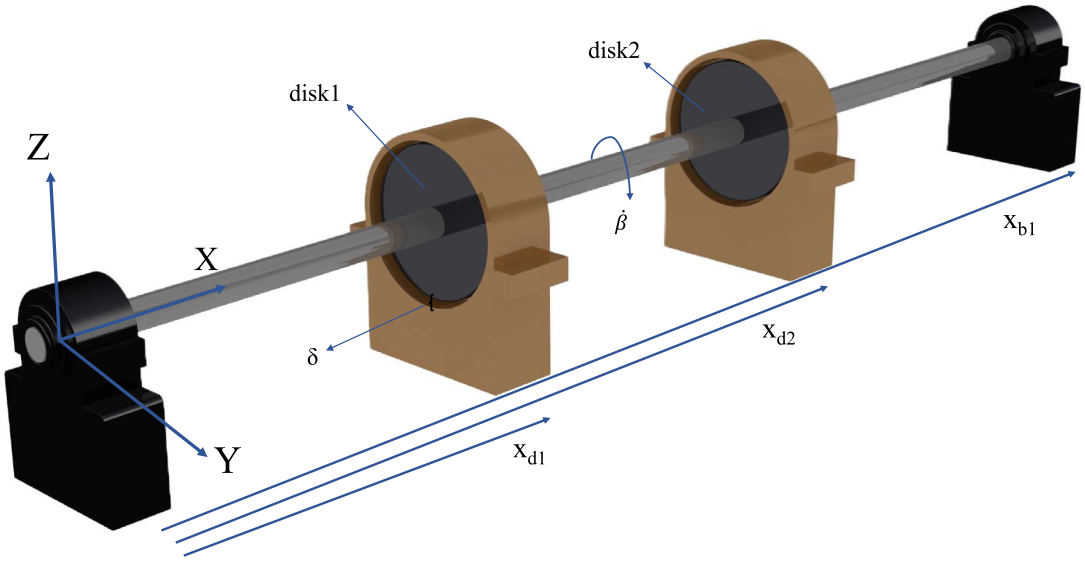

Fig. 1. Schematic diagram of the rotor-disk-bearing system.

Parameters	Definition	Parameters	Definition
M_{ud1}	Unbalance mass of disk 1	M_{d2}	Mass of disk 2
M_{ud2}	Unbalance mass of disk 2	$v(x, t)$	Displacement in the z-axis
I	Moment of inertia of shaft	$w(x, t)$	Displacement in the y-axis
I_{21}	Diametrical mass moment of inertia of disk 1	K_h	Radial stiffnesses of the stator
I_{22}	Diametrical mass moment of inertia of disk 2	K_l	Linear stiffnesses of the bearings
I_{11}	Polar mass moment of inertia of disk 1	K_{nl}	Nonlinear stiffnesses of the bearings
I_{12}	Polar mass moment of inertia of disk 2	C_b	Damping of the bearings
$\dot{\beta}$	Shaft rotational speed	C_r	Damping of the shaft
r_1	Eccentricity of the disk 1 unbalance	ρ	Mass density of shaft
r_2	Eccentricity of the disk 2 unbalance	A	Shaft cross-sectional area
M_{d1}	Mass of disk 1	E	Young's modulus of elasticity of the shaft

Table 1. List of parameters.

Modeling and derivation of governing equations

Figure 1 illustrates the schematic diagram of the rotor-disk-bearing system. Since the operational speed of most rotors exceeds the first critical speed and may even surpass the second or third, analyzing the system's behavior during its passage through these critical speeds is essential. For this purpose, non-stationary analysis proves highly beneficial in comparison with stationary analyses, as it enables the prediction of the system's response from startup up to the maximum rotational velocity, especially as it traverses the critical speeds.

After deriving the kinetic and potential energies of the system components and applying Hamilton's principle, the equations of motion are obtained. These equations are then discretized using the Galerkin method. The physical properties of the system are provided in Table1.

The kinetic energy of the system components

To derive the dynamic equations of motion, the terms of the flexible rotor, rigid disks, and the unbalanced masses must first be calculated[3]. These terms are then inserted into Hamilton's principle, which leads to the formulation of the partial differential equations governing the system's motion.

$$T_r = \int_0^L \left(\frac{\rho A}{2}\left(\dot{v}^2 + \dot{w}^2\right)\right) dx + \int_0^L \left(\frac{\rho I}{2}\left(\dot{\alpha}^2 + \dot{\theta}^2\right)\right) dx + \int_0^L \left(2\rho I(\dot{\alpha}\dot{\beta}\theta + \dot{\beta}^2)\right) dx \quad (1)$$

$$T_{d1} = \frac{1}{2}M_{d1}\int_0^L \left(\dot{v}^2 + \dot{w}^2\right)\delta(x - L_{d1})\, dx + \frac{1}{2}\int_0^L \left(I_{21}\left(\dot{\alpha}^2 + \dot{\theta}^2\right) + I_{11}\dot{\beta}^2 + I_{11}\dot{\alpha}\dot{\beta}\theta\right)\delta(x - L_{d1})\, dx \quad (2)$$

$$T_{d2} = \frac{1}{2} M_{d2} \int_0^L \left(\dot{v}^2 + \dot{w}^2\right) \delta(x - L_{d2})\, dx + \frac{1}{2} \int_0^L \left(I_{22}\left(\dot{\alpha}^2 + \dot{\theta}^2\right) + I_{12}\dot{\beta}^2 + I_{12}\dot{\alpha}\dot{\beta}\theta\right) \delta(x - L_{d2})\, dx \quad (3)$$

$$T_{ud1} = \frac{1}{2} \int_0^L \left(M_{ud1} r_1^2 \Omega^2 + M_{ud1} r_1 \Omega \dot{w} \cos(\Omega t) - M_{ud1} r_1 \Omega \dot{v} \sin(\Omega t)\right) \delta(x - L_{d1})\, dx \quad (4)$$

$$T_{ud2} = \frac{1}{2} \int_0^L \left(M_{ud2} r_2^2 \Omega^2 + M_{ud2} r_2 \Omega \dot{w} \cos(\Omega t) - M_{ud2} r_2 \Omega \dot{v} \sin(\Omega t)\right) \delta(x - L_{d2})\, dx \quad (5)$$

In the above equations, T_r represents the **kinetic energy of the shaft**, T_{d1} and T_{d2} denote the **kinetic energies of disks 1 and 2**, and T_{ud1}, T_{ud2} correspond to the **kinetic energies of the unbalanced masses**. The displacement $v(x,t)$ represents the lateral vibrations of the system in the z-direction, while $w(x,t)$ represents the displacement in the y-direction. Where $\dot{\beta}$ denotes the angular velocity of the shaft ($\dot{\beta} = \Omega$). Additionally, $\dot{\alpha}$ is given by:

$$\dot{\alpha} = \frac{\partial}{\partial t}\left(\frac{\partial v}{\partial x}\right),$$

and $\dot{\theta}$ is given by:

$$\dot{\theta} = \frac{\partial}{\partial t}\left(\frac{\partial w}{\partial x}\right).$$

Potential energy of the shaft

To derive the equations of motion, the potential energy of both the shaft and the disks is also required. The potential energy of the disks is considered to be zero due to the assumption that they are rigid. This is because, within the system's frequency excitation range, the natural frequencies of the first disk are significantly higher than the first natural frequency of the rotor system and also exceed the uppermost operational rotational velocity of the rotor, indicating that the disk does not vibrate but only exhibits rigid-body dynamic motion[40]. The potential energy of the shaft, accounting for the contribution of nonlinear terms arising from geometric nonlinearity of the von Karman type, is obtained according to the following relations[3]:

$$U_s = \int_0^L \left(\frac{EI}{2}\left(\left(\frac{\partial}{\partial x}\left(\frac{\partial v}{\partial x}\right)\right)^2 + \left(\frac{\partial}{\partial x}\left(\frac{\partial w}{\partial x}\right)\right)^2\right)\right) dx + \int_0^L \left(\frac{EA}{8}\left(\left(\frac{\partial v}{\partial x}\right)^4 + \left(\frac{\partial w}{\partial x}\right)^4 + 2\left(\frac{\partial v}{\partial x}\right)^2\left(\frac{\partial w}{\partial x}\right)^2\right)\right) dx \quad (6)$$

Potential energy of the flexible bearings

The modeling of the bearings is carried out using a linear and a nonlinear springs. In this method, instead of applying the force of each ball, which varies with time and the rotational speed of the shaft[10], an equivalent spring and damper are used Fig.2. The difference between these two methods is that in the spring-damper model of the bearings, the force is applied to the shaft regardless of its rotational speed, whereas in the Hertzian theory

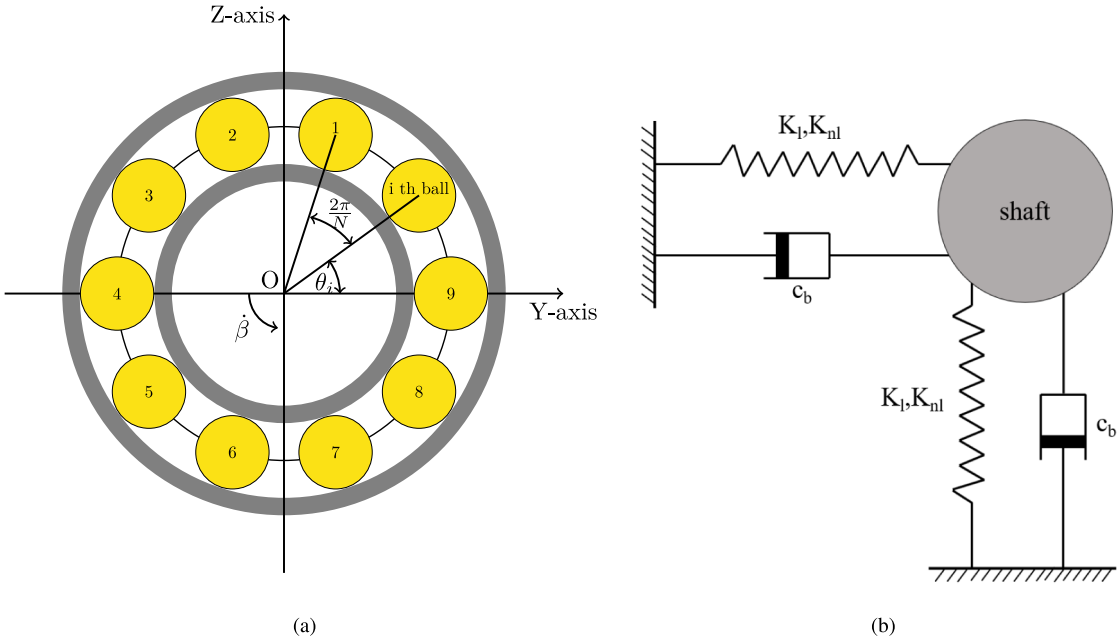

Fig. 2. (**a**) Schematic diagram of the ball bearing, (**b**) Spring and damper model.

model, an asymmetric force is applied to the shaft. Therefore, the potential energy of the bearings is calculated using the following relation[3]:

$$U_b = \frac{1}{2}\int_0^l \left(v\left(K_l v + K_{nl} v^3\right) + w\left(K_l w + K_{nl} w^3\right)\delta(x - L_{d1})\right) dx + \frac{1}{2}\int_0^l \left(v\left(K_l v + K_{nl} v^3\right) + w\left(K_l w + K_{nl} w^3\right)\delta(x - L_{d2})\right) dx \quad (7)$$

The work done by non-conservative forces

The work resulting from non-conservative forces, including the bearings and the shaft damping force, is obtained[3] as:

$$\begin{aligned} W_{nc} = \frac{1}{2}\int_0^l C_r \begin{pmatrix} \dot{w} \\ \dot{v} \end{pmatrix}^T \begin{pmatrix} dw \\ dv \end{pmatrix} dx + \frac{1}{2}\int_0^l C_{b1} \begin{pmatrix} \dot{w} \\ \dot{v} \end{pmatrix}^T \begin{pmatrix} dw \\ dv \end{pmatrix} dx\, \delta(x - L_{d1}) \\ + \frac{1}{2}\int_0^l C_{b2} \begin{pmatrix} \dot{w} \\ \dot{v} \end{pmatrix}^T \begin{pmatrix} dw \\ dv \end{pmatrix} dx\, \delta(x - L_{d2}) \end{aligned} \quad (8)$$

Rub phenomenon and associated forces

Rub impact occurs when the rotor comes into contact with the stator, leading to nonlinear interactions that affect the system's vibration characteristics. This contact generates two primary forces: Normal Force: A force perpendicular to the contact surface, resulting from the impact between the rotor and stator.Tangential Force: A frictional force parallel to the contact surface, caused by the relative motion between the rotor and stator. Figure 3 illustrates these forces clearly. These forces introduce nonlinearities into the system, leading to complex dynamic behaviors such as subharmonic vibrations, chaotic motion, and even rotor instability. The normal and tangential forces due to rub are modeled as follows[35]:

$$F_{ni} = K_{hi}\left(\sqrt{v^2 + w^2} - \delta_i\right) H\left(\sqrt{v^2 + w^2} - \delta_i\right)\delta(x - x_{di}) \quad (9)$$

$$F_{\tau i} = \mu_i F_{ni}, \quad i = 1, 2 \quad (10)$$

where:

- F_{ni} is the normal impact force at disk positions,
- $F_{\tau i}$ is the frictional force,
- K_{hi} is the radial stiffness of the stator,
- δ_i is the clearance between the rotor and stator,
- $H(x)$ is the Heaviside function, and
- μ_i is the friction coefficient.

Expressing these forces in the *y*-*z* coordinates:

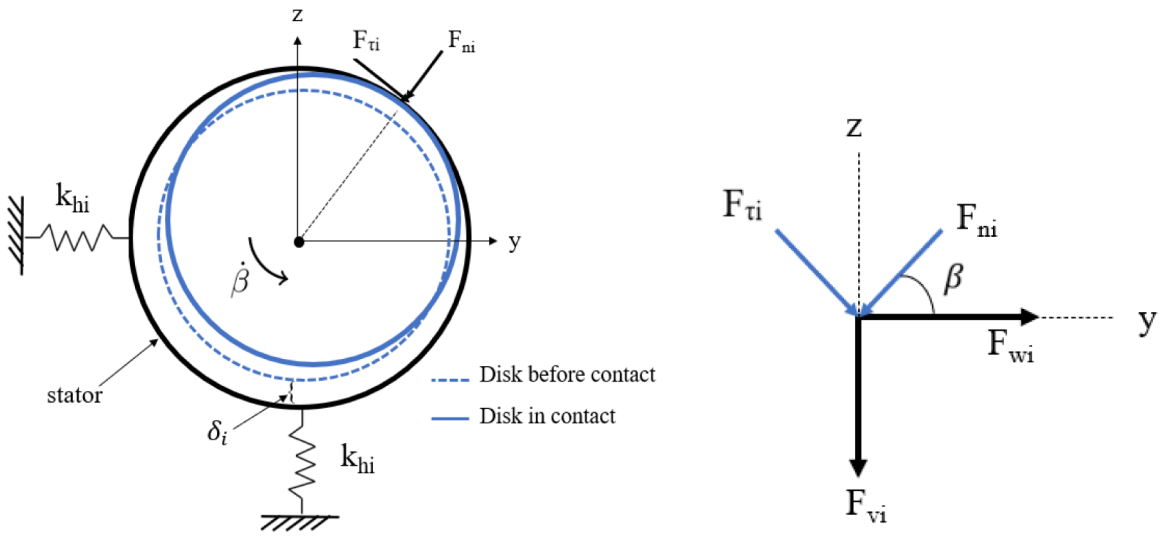

Fig. 3. (**a**) Collision between the disk, (**b**) stator and the corresponding forces decomposition at the contact point.

$$F_{wi} = K_{hi}\left(\sqrt{v^2+w^2}-\delta_i\right) H\left(\sqrt{v^2+w^2}-\delta_i\right) \frac{\mu_i v - w}{\sqrt{v^2+w^2}}\,\delta(x-x_{di}) \tag{11}$$

$$F_{vi} = -K_{hi}\left(\sqrt{v^2+w^2}-\delta_i\right) H\left(\sqrt{v^2+w^2}-\delta_i\right) \frac{\mu_i w + v}{\sqrt{v^2+w^2}}\,\delta(x-x_{di}) \tag{12}$$

$$F_{bi} = \mu_i K_{hi}\left(\sqrt{v^2+w^2}-\delta_i\right) H\left(\sqrt{v^2+w^2}-\delta_i\right) \sqrt{v^2+w^2}\,\delta(x-x_{di}) \tag{13}$$

Extraction of the equations

After deriving the kinetic energies of the shaft, disks, and unbalanced masses, as well as the potential energies of the shaft and bearings, and considering the damping and rub forces, all these expressions are then substituted into the extended Hamilton's principle to derive the equations of motion.

$$\delta \int_0^t (T_{total} - U_{total} + W_{nc})\, dt = 0 \tag{14}$$

To convert the PDEs extracted in the previous section, which contain both time and spatial derivatives, into ODEs with only time derivatives, the Galerkin method is applied. For this purpose, the mode shape of a beam on two spring supports is used, which resembles the rotor-bearing system witch presented in Appendix. In the first three flexible modes, this mode shape starts to oscillate with a value greater than zero at boundaries, while for a rigid support, the displacement at the boundary conditions remains zero Fig. 4. Only the first mode of the beam is utilized for discretizing the equations with the Galerkin method, as the first critical speed holds significant importance in the design and analysis of rotary systems. This approach is based on considering the system's response in both directions as a function of time, the mode shape of the beam on the two spring supports, and the orthogonality property of the mode shapes.

$$w(x,t) = \phi(x)\, W(t) \tag{15}$$

$$v(x,t) = \phi(x)\, V(t) \tag{16}$$

equations of motion

The coupled bending-torsional equations of motion of the rotor, obtained using the Galerkin method, are presented as Eqs. (17)–(19). Equations (17)–(18) correspond to the bending vibrations, while Eq. (19) represents the torsional vibration of the system.

$$\ddot{w} + C\dot{w} + k_1\dot{\beta}\dot{v} + k_2 w + k_3\ddot{\beta}v - \mu v^2 w - k_4 w^3 = \Lambda_1\dot{\beta}^2\cos(\beta) + \Lambda_2\ddot{\beta}\sin(\beta) - \varphi(x=x_{d1})\frac{F_{w1}}{M} - \varphi(x=x_{d2})\frac{F_{w2}}{M} \tag{17}$$

$$\ddot{v} + C\dot{v} - k_1\dot{\beta}\dot{w} + k_2 v - k_3\ddot{\beta}w - \mu w^2 v - k_4 v^3 = \Lambda_1\dot{\beta}^2\sin(\beta) - \Lambda_2\ddot{\beta}\cos(\beta) + \varphi(x=x_{d1})\frac{F_{v1}}{M} + \varphi(x=x_{d2})\frac{F_{v2}}{M} \tag{18}$$

$$\ddot{\beta} + m_2\dot{v}\dot{w} + m_2 w\ddot{v} + m_4\ddot{v}\cos(\beta) - m_4\ddot{w}\sin(\beta) + e_0\varphi(x=x_{d1})\frac{F_{b1}}{M} + e_0\varphi(x=x_{d2})\frac{F_{b2}}{M} = e_0 E \tag{19}$$

The excitation source of the system is non-ideal. In the ideal case, the torque applied by the motor remains constant. However, for a more accurate and realistic model, it is assumed that the applied torque decreases as the rotational speed of the rotor decreases as shown in Fig. 5. E represents the torque applied by the motor to the rotating system, which is not a constant value[33] The terms $C\dot{w}$ and $C\dot{v}$ represent linear damping, while $k_1\dot{\beta}\dot{v}$ and $k_1\beta\dot{w}$ correspond to the gyroscopic effect. The expressions $-\mu v^2 w - v_4 w^3$ and $-\mu w^2 v - v_4 v^3$ arise from the geometric nonlinearities of the shaft. Additionally, the sinusoidal and cosine terms on the right-hand side of

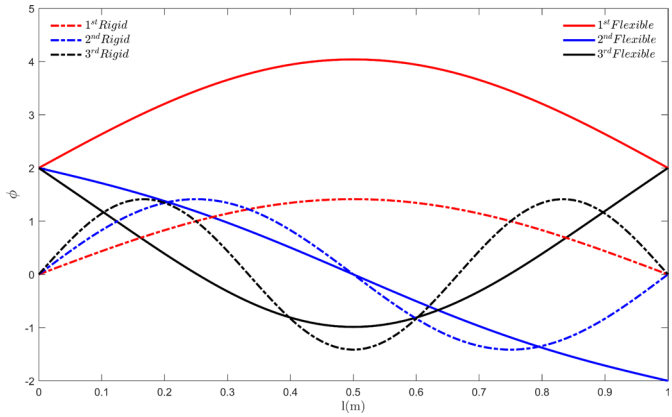

Fig. 4. Mode shapes of a beam with rigid and elastic supports ($\gamma_1 = 2.56, \gamma_2 = 3.74, \gamma_3 = 5.32$).

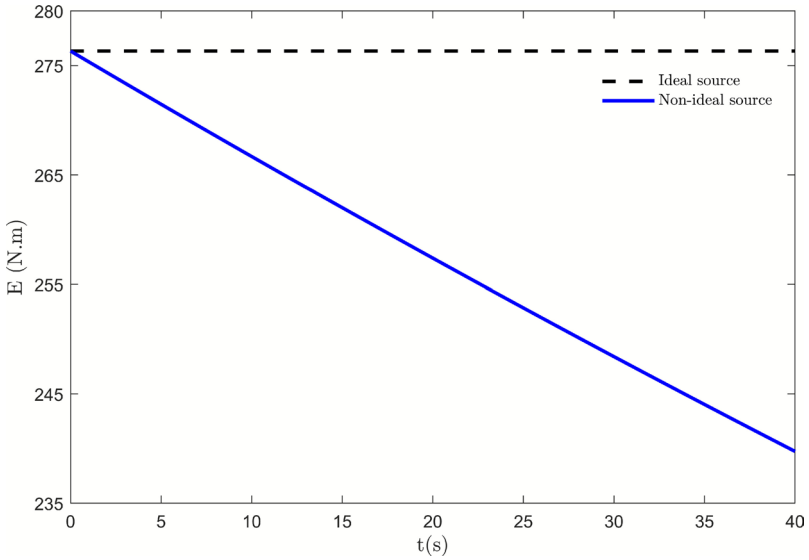

Fig. 5. Performance comparison of ideal and non-ideal excitation sources.

Parameter	Value	Parameter	Value
Young's modulus (E)	200 GPa	Shaft length (L)	1.00 m
Shaft damping (C_r)	100 Ns/m	Shaft radius (R)	0.020 m
Bearing damping (C_b)	10 Ns/m	Friction coefficient (μ)	0.2 –
Bearing linear stiffness (k_l)	9×10^5 N/m	Disk diameter (D)	0.180 m
Bearing nonlinear stiffness (k_{nl})	2×10^9 N/m	Disk thickness (h)	0.015 m
Density (ρ)	7800 kg/m^3	Unbalanced mass ($M_{ud1,2}$)	0.015 kg
Stator radial stiffness (k_h)	1.2×10^4 N/m	Eccentricity (r_1)	0.070 m
Stator clearance (δ)	3×10^{-4} m	Eccentricity (r_2)	0.070 m
Torque reduction coefficient (E_1)	0.035 N m	Applied torque(E_0)	276 N.m

Table 2. Parameter values for the rotor-disk-bearing system.

the equations indicate the unbalance forces resulting from the eccentric masses mounted on the disks and The forces F_v, F_w, and F_b are caused by the interaction between the disk and the stator. Equation (20) denotes the torque applied to the system, indicating a non-ideal linear excitation source. All the physical and geometrical parameters used in the modeling are listed in Table2.

$$E = E_0 - E_1\dot{\beta} \tag{20}$$

Some parameters in the ODEs of motion are obtained by applying the Galerkin method to the governing PDEs, as follows:

$$\begin{aligned} M = {} & M_{d1}\phi^2(x)\big|_{x=l_{d1}} + M_{d2}\phi^2(x)\big|_{x=l_{d2}} - I_{21}\phi(x)\frac{\partial^2\phi(x)}{\partial x^2}\Big|_{x=l_{d1}} - I_{22}\phi(x)\frac{\partial^2\phi(x)}{\partial x^2}\Big|_{x=l_{d2}} \\ & - \rho A\int_0^l \phi(x)\frac{\partial^2\phi(x)}{\partial x^2}\,dx + \rho I\int_0^l \phi(x)\frac{\partial^2\phi(x)}{\partial x^2}\,dx \end{aligned} \tag{21}$$

$$k_1 = \frac{1}{M}\left(I_{11}\phi(x)\frac{\partial^2}{\partial x^2}\phi(x)\bigg|_{x=l_{d1}} + I_{12}\phi(x)\frac{\partial^2}{\partial x^2}\phi(x)\bigg|_{x=l_{d2}} + 2\rho I\int_0^l \phi(x)\frac{\partial^2}{\partial x^2}\phi(x)\,dx\right). \tag{22}$$

$$k_2 = \frac{EI}{M}\int_0^l \phi(x)\frac{\partial^4}{\partial x^4}\phi(x)\,dx + \frac{K_l\phi^2(x)\big|_{x=0} + K_l\phi^2(x)\big|_{x=l}}{M}. \tag{23}$$

$$\mu = \frac{3}{2}M\left(EA\int_0^l \phi(x)\frac{\partial^2}{\partial x^2}\phi(x)\frac{\partial}{\partial x}\phi(x)\,dx\right). \tag{24}$$

$$k_4 = \frac{3}{2}M\left(EA\int_0^l \phi(x)\frac{\partial^2}{\partial x^2}\phi(x)\frac{\partial}{\partial x}\phi(x)\,dx\right) - \frac{2K_{nl}}{M}\left(\phi^4(x)\big|_{x=0} + \phi^4(x)\big|_{x=l}\right). \tag{25}$$

$$C = \frac{c_r + \left(\phi^2(x)\big|_{x=0} + \phi^2(x)\big|_{x=l}\right)c_b}{M}, \quad \Lambda_1 = \frac{M_{ud1}\Omega^2 r_1\phi(l_{d1})}{M}, \quad \Lambda_2 = \frac{M_{ud2}\Omega^2 r_2\phi(l_{d2})}{M}. \tag{26}$$

$$m_2 = \frac{\left(\frac{d}{dx}I_{11}\phi\left(\frac{\partial}{\partial x}\phi\right)^2\Big|_{x=l_{d1}} + \frac{d}{dx}I_{12}\phi\left(\frac{\partial}{\partial x}\phi\right)^2\Big|_{x=l_{d2}} + 2\rho I\int_0^l \phi\left(\frac{\partial}{\partial x}\phi\right)^2 dx\right)}{I_{11}\phi\Big|_{x=l_{d1}} + I_{12}\phi\Big|_{x=l_{d2}} + M_{ud1}r_1^2\phi\Big|_{x=l_{d1}} + M_{ud2}r_2^2\phi\Big|_{x=l_{d2}} + 2\rho I\int_0^l \phi\,dx}. \tag{27}$$

$$m_4 = \frac{M_{ud1}r_1\phi^2\big|_{x=l_{d1}} + M_{ud2}r_2\phi^2\big|_{x=l_{d2}}}{I_{11}\phi\big|_{x=l_{d1}} + I_{12}\phi\big|_{x=l_{d2}} + M_{ud1}r_1^2\phi\big|_{x=l_{d1}} + M_{ud2}r_2^2\phi\big|_{x=l_{d2}} + 2\rho I\int_0^l \phi\,dx}. \tag{28}$$

$$e_0 = \frac{1}{I_{11}\phi\big|_{x=l_{d1}} + I_{12}\phi\big|_{x=l_{d2}} + M_{ud1}r_1^2\phi\big|_{x=l_{d1}} + M_{ud2}r_2^2\phi\big|_{x=l_{d2}} + 2\rho I\int_0^l \phi\,dx}. \tag{29}$$

Analytical solution of the equations using the averaging method

In this section, we aim to obtain analytical solutions for the system using the method of averaging. This method is particularly advantageous for analyzing nonlinear dynamical systems, as it allows for the reduction of complex equations into simpler forms by averaging over fast oscillations.One significant advantage of the averaging method, as employed in this study, is its flexibility in handling equations that involve discontinuities or non-smooth components an aspect where methods such as multiple scales or asymptotic expansions often fall short. It provides insight into the long-term behavior of the system and is especially useful when dealing with weakly nonlinear problems. Among the most significant analytical methods are those based on averaging techniques[41]. Typically, solutions derived from these methods begin with a parameter transformation, which converts the dependent variables into a new set of independent variables.To solve the equations using the averaging method, the second-order equations of motion are reduced to first-order ones, as shown in Eqs. (30)–(34).

$$x_1 = w, \tag{30}$$

$$x_2 = \dot{w}, \tag{31}$$

$$y_1 = v, \tag{32}$$

$$y_2 = \dot{v}, \tag{33}$$

$$\Omega = \dot{\beta}. \tag{34}$$

Due to the relatively small contributions of geometric nonlinearities, damping effects, and unbalance[33] the values of $\ddot{\beta}, C, \mu, k_4, \Lambda_1$, and Λ_2 can be replaced with the expressions $\epsilon C, \epsilon\ddot{\beta}, \epsilon\mu, \epsilon k_4, \epsilon\Lambda_1$,and$\epsilon\Lambda_2$. After substituting these expressions and performing the variable transformation as described, the three second-order equations of motion are converted into six first-order equations.

$$\begin{aligned}\dot{x}_1 &= x_2\\ \dot{x}_2 &= -\varepsilon C x_2 - k_1\Omega y_2 - k_2 x_1 - k_3\dot{\Omega}y_1 + \varepsilon\mu y_1^2 x_1 + \varepsilon k_4 x_1^3 + \varepsilon\Lambda_1\Omega^2\cos(\beta) + \varepsilon\Lambda_2\dot{\Omega}\sin(\beta)\end{aligned} \tag{35}$$

$$- \varphi(x = x_{d1})\frac{F_{w1}}{M} - \varphi(x = x_{d2})\frac{F_{w2}}{M} \tag{36}$$

$$\dot{y}_1 = y_2 \tag{37}$$

$$\begin{aligned}\dot{y}_2 &= -\varepsilon C y_2 + k_1\Omega x_2 - k_2 y_1 + k_3\dot{\Omega}x_1 + \varepsilon\mu x_1^2 y_1 + \varepsilon k_4 y_1^3 + \varepsilon\Lambda_1\Omega^2\sin(\beta)\\ &\quad + \varepsilon\Lambda_2\dot{\Omega}\cos(\beta) + \varphi(x = x_{d1})\frac{F_{v1}}{M} + \varphi(x = x_{d2})\frac{F_{v2}}{M}\end{aligned} \tag{38}$$

$$\dot{\beta} = \Omega \tag{39}$$

$$\begin{aligned}\dot{\Omega} &= -m_2 x_2 y_2 - m_2 x_1\dot{y}_2 - m_4\dot{y}_2\cos(\beta) + m_4\dot{x}_2\sin(\beta) + e_0 E(\Omega)\\ &\quad - e_0\varphi(x = x_{d1})\frac{F_{b1}}{M} - e_0\varphi(x = x_{d2})\frac{F_{b2}}{M}\end{aligned} \tag{40}$$

The complexity of coupled nonlinear differential equations, where closed-form analytical solutions are generally intractable, necessitates a simplifying transformation through new state variables[41]:

$$x_1 = a_1\cos(\beta + \psi_1), \tag{41}$$

$$x_2 = -a_1\Omega\sin(\beta+\psi_1), \tag{42}$$

$$y_1 = a_2\cos(\beta+\psi_2), \tag{43}$$

$$y_2 = -a_2\Omega\sin(\beta+\psi_2), \tag{44}$$

Substituting Eqs. (41)–(44) into Eqs. (35)–(40) and simplifying yields:

$$\begin{aligned}\dot{a}_1 + a_1\frac{\dot{\Omega}}{\Omega}\sin^2(\beta+\psi_1) = {} & \frac{k_2-\Omega^2}{2\Omega}a_1\sin(2\beta+2\psi_1) - \varepsilon C a_1\sin^2(\beta+\psi_1) - \varepsilon\Lambda_1\Omega\cos(\beta)\sin(\beta+\psi_1)\\ & - k_1\Omega a_2\sin(\beta+\psi_1)\sin(\beta+\psi_2) - \frac{\varepsilon a_2^2 a_1\mu}{2\Omega}\cos^2(\beta+\psi_2)\sin(2\beta+2\psi_1)\\ & - \frac{\varepsilon a_1^3 k_4}{2\Omega}\cos^2(\beta+\psi_1)\sin(2\beta+2\psi_1) + \varepsilon a_2 k_3\frac{\dot{\Omega}}{\Omega}\cos(\beta+\psi_2)\sin(\beta+\psi_1)\\ & + \varphi(x=x_{d1})\frac{F_{w1}}{\Omega M}\sin(\beta+\psi_1) + \varphi(x=x_{d2})\frac{F_{w2}}{\Omega M}\sin(\beta+\psi_1),\end{aligned} \tag{45}$$

$$\begin{aligned}\dot{a}_2 + a_2\frac{\dot{\Omega}}{\Omega}\sin^2(\beta+\psi_2) = {} & \frac{k_2-\Omega^2}{2\Omega}a_2\sin(2\beta+2\psi_2) - \varepsilon C a_2\sin^2(\beta+\psi_2) - \varepsilon\Lambda_1\Omega\sin(\beta)\sin(\beta+\psi_2)\\ & + k_1\Omega a_1\sin(\beta+\psi_2)\sin(\beta+\psi_1) - \frac{\varepsilon a_1^2 a_2\mu}{2\Omega}\cos^2(\beta+\psi_1)\sin(2\beta+2\psi_2)\\ & - \frac{\varepsilon a_2^3 k_4}{2\Omega}\cos^2(\beta+\psi_2)\sin(2\beta+2\psi_2) - \varepsilon a_1 k_3\frac{\dot{\Omega}}{\Omega}\cos(\beta+\psi_1)\cos(\beta+\psi_2)\\ & - \varphi(x=x_{d1})\frac{F_{v1}}{\Omega M}\sin(\beta+\psi_2) - \varphi(x=x_{d2})\frac{F_{v2}}{\Omega M}\sin(\beta+\psi_2),\end{aligned} \tag{46}$$

$$\begin{aligned}a_1\left(\dot{\psi}_1 + \frac{\dot{\Omega}}{2\Omega}\sin(2\beta+2\psi_1)\right) = {} & \frac{k_2-\Omega^2}{\Omega}a_1\cos^2(\beta+\psi_1) - \frac{\varepsilon C a_1}{2}\sin(2\beta+2\psi_1)\\ & - \varepsilon\Lambda_1\Omega\cos(\beta)\cos(\beta+\psi_1) - \frac{\varepsilon a_1^3 k_4}{\Omega}\cos^4(\beta+\psi_1)\\ & - k_1\Omega a_2\cos(\beta+\psi_1)\sin(\beta+\psi_2) + \varepsilon a_2 k_3\frac{\dot{\Omega}}{\Omega}\cos(\beta+\psi_2)\cos(\beta+\psi_1)\\ & - \frac{\varepsilon a_2^2 a_1\mu}{\Omega}\cos^2(\beta+\psi_2)\cos^2(\beta+\psi_1)\\ & + \varphi(x=x_{d1})\frac{F_{w1}}{\Omega M}\cos(\beta+\psi_1) + \varphi(x=x_{d2})\frac{F_{w2}}{\Omega M}\cos(\beta+\psi_1),\end{aligned} \tag{47}$$

$$\begin{aligned}a_2\left(\dot{\psi}_2 + \frac{\dot{\Omega}}{2\Omega}\sin(2\beta+2\psi_2)\right) = {} & \frac{k_2-\Omega^2}{\Omega}a_2\cos^2(\beta+\psi_2) - \frac{\varepsilon C a_2}{2}\sin(2\beta+2\psi_2)\\ & - \varepsilon\Lambda_1\Omega\sin(\beta)\cos(\beta+\psi_2) - \frac{\varepsilon a_2^3 k_4}{\Omega}\cos^4(\beta+\psi_2)\\ & + k_1\Omega a_1\cos(\beta+\psi_2)\sin(\beta+\psi_1) - \varepsilon a_1 k_3\frac{\dot{\Omega}}{\Omega}\cos(\beta+\psi_1)\cos(\beta+\psi_2)\\ & - \frac{\varepsilon a_1^2 a_2\mu}{\Omega}\cos^2(\beta+\psi_2)\cos^2(\beta+\psi_1)\\ & - \varphi(x=x_{d1})\frac{F_{v1}}{\Omega M}\cos(\beta+\psi_2) - \varphi(x=x_{d2})\frac{F_{v2}}{\Omega M}\cos(\beta+\psi_2).\end{aligned} \tag{48}$$

$$\begin{aligned}\dot{\Omega} = {} & \varepsilon m_2 a_1 a_2\sin(\beta+\psi_1)\sin(\beta+\psi_2) - \varepsilon m_2\Big[-a_1\dot{a}_2\Omega\sin(\psi_2)\cos(\psi_1)\\ & - a_1 a_2\dot{\Omega}\sin(\psi_2)\cos(\psi_1) - a_1 a_2\Omega^2\cos(\psi_2)\cos(\psi_1) - a_1 a_2\Omega\dot{\psi}_2\cos(\psi_2)\cos(\psi_1)\Big]\\ & + \varepsilon m_4\cos(\beta)\Big[\dot{a}_2\Omega\sin(\psi_2) + a_2\dot{\Omega}\sin(\psi_2) + a_2\Omega^2\cos(\psi_2) + a_2\Omega\dot{\psi}_2\cos(\psi_2)\Big]\\ & + \varepsilon m_4\sin(\beta)\Big[-\dot{a}_1\Omega\sin(\psi_1) - a_1\dot{\Omega}\sin(\psi_1) - a_1\Omega^2\cos(\psi_1) - a_1\Omega\dot{\psi}_1\cos(\psi_1)\Big]\\ & + \varepsilon e_0 E - e_0\varphi(x=x_{d1})\frac{F_{b1}}{M} - e_0\varphi(x=x_{d2})\frac{F_{b2}}{M}.\end{aligned} \tag{49}$$

The system of equations presented above is formulated in terms of the independent variables $a_1, a_2, \psi_1, \Omega, \beta$, and ψ_2. Although the system comprises five independent equations and six unknowns, the interdependence among the equations renders a direct solution in this form unattainable. Nevertheless, this challenge can be overcome by applying an averaging process over the periodic interval 2π, which effectively eliminates the variable β from the system. As a result, the system reduces to five equations in five unknowns, enabling the possibility of a consistent solution.

$$
\begin{aligned}
\dot{a}_1 + \frac{a_1\dot{\Omega}}{2\Omega} &= -\frac{1}{2}\varepsilon\Lambda_1\Omega\sin(\psi_1) - \frac{1}{2}\varepsilon C a_1 + \frac{\varepsilon k_3 a_2\dot{\Omega}}{2\Omega}\sin(\psi_1-\psi_2) \\
&\quad - \frac{1}{8}\varepsilon\mu a_2^2 a_1\sin(2\psi_1-2\psi_2) - \frac{1}{2}k_1 a_2\Omega\cos(\psi_1-\psi_2) \\
&\quad + \frac{1}{2\pi\Omega M}\int_0^{2\pi} K_{h1}\left(\sqrt{a_2^2\cos^2(\beta+\psi_2)\phi^2(x_{d1}) + a_1^2\cos^2(\beta+\psi_1)\phi^2(x_{d1})} - \delta_1\right) \\
&\quad \times H\left(\sqrt{a_2^2\cos^2(\beta+\psi_2)\phi^2(x_{d1}) + a_1^2\cos^2(\beta+\psi_1)\phi^2(x_{d1})} - \delta_1\right) \\
&\quad \times \frac{\mu a_2\cos(\beta+\psi_2) - a_1\cos(\beta+\psi_1)}{\sqrt{a_2^2\cos^2(\beta+\psi_2) + a_1^2\cos^2(\beta+\psi_1)}}\cdot\phi^2(x_{d1})\sin(\beta+\psi_1)\,d\beta \\
&\quad + \frac{1}{2\pi\Omega M}\int_0^{2\pi} K_{h2}\left(\sqrt{a_2^2\cos^2(\beta+\psi_2)\phi^2(x_{d2}) + a_1^2\cos^2(\beta+\psi_1)\phi^2(x_{d2})} - \delta_2\right) \\
&\quad \times H\left(\sqrt{a_2^2\cos^2(\beta+\psi_2)\phi^2(x_{d2}) + a_1^2\cos^2(\beta+\psi_1)\phi^2(x_{d2})} - \delta_2\right) \\
&\quad \times \frac{\mu a_2\cos(\beta+\psi_2) - a_1\cos(\beta+\psi_1)}{\sqrt{a_2^2\cos^2(\beta+\psi_2) + a_1^2\cos^2(\beta+\psi_1)}}\cdot\phi^2(x_{d2})\sin(\beta+\psi_1)\,d\beta
\end{aligned} \tag{50}
$$

$$
\begin{aligned}
\dot{a}_2 + \frac{a_2\dot{\Omega}}{2\Omega} &= -\frac{1}{2}\varepsilon\Lambda_1\Omega\cos(\psi_1) - \frac{1}{2}\varepsilon C a_2 - \frac{\varepsilon k_3 a_1\dot{\Omega}}{2\Omega}\cos(\psi_1-\psi_2) \\
&\quad + \frac{1}{8}\varepsilon\mu a_1^2 a_2\sin(2\psi_1-2\psi_2) + \frac{1}{2}k_1 a_1\Omega\cos(\psi_1-\psi_2) \\
&\quad - \frac{1}{2\pi\Omega M}\int_0^{2\pi} K_{h1}\left(\sqrt{a_2^2\cos^2(\beta+\psi_2)\phi^2(x_{d1}) + a_1^2\cos^2(\beta+\psi_1)\phi^2(x_{d1})} - \delta_1\right) \\
&\quad \times H\left(\sqrt{a_2^2\cos^2(\beta+\psi_2)\phi^2(x_{d1}) + a_1^2\cos^2(\beta+\psi_1)\phi^2(x_{d1})} - \delta_1\right) \\
&\quad \times \frac{a_2\cos(\beta+\psi_2) + \mu a_1\cos(\beta+\psi_1)}{\sqrt{a_2^2\cos^2(\beta+\psi_2) + a_1^2\cos^2(\beta+\psi_1)}}\cdot\phi^2(x_{d1})\sin(\beta+\psi_2)\,d\beta \\
&\quad - \frac{1}{2\pi\Omega M}\int_0^{2\pi} K_{h2}\left(\sqrt{a_2^2\cos^2(\beta+\psi_2)\phi^2(x_{d2}) + a_1^2\cos^2(\beta+\psi_1)\phi^2(x_{d2})} - \delta_2\right) \\
&\quad \times H\left(\sqrt{a_2^2\cos^2(\beta+\psi_2)\phi^2(x_{d2}) + a_1^2\cos^2(\beta+\psi_1)\phi^2(x_{d2})} - \delta_2\right) \\
&\quad \times \frac{a_2\cos(\beta+\psi_2) + \mu a_1\cos(\beta+\psi_1)}{\sqrt{a_2^2\cos^2(\beta+\psi_2) + a_1^2\cos^2(\beta+\psi_1)}}\cdot\phi^2(x_{d2})\sin(\beta+\psi_2)\,d\beta
\end{aligned} \tag{51}
$$

$$
\begin{aligned}
a_1\dot{\psi}_1 &= \frac{k_2-\Omega^2}{2\Omega}a_1 - \frac{1}{2}\varepsilon\Lambda_1\Omega\cos(\psi_1) + \frac{1}{2}k_1 a_2\Omega\sin(\psi_1-\psi_2) \\
&\quad - \frac{3\varepsilon}{8\Omega}a_1^3 k_4 - \frac{\varepsilon}{4\Omega}(a_1a_2)^2\mu - \frac{\varepsilon}{8\Omega}(a_1a_2)^2\mu\cos(2\psi_1-2\psi_2) \\
&\quad + \frac{\varepsilon k_3 a_2\dot{\Omega}}{2\Omega}\cos(\psi_1-\psi_2) \\
&\quad + \frac{1}{2\pi\Omega M}\int_0^{2\pi} K_{h1}\left(\sqrt{a_2^2\cos^2(\beta+\psi_2)\phi^2(x_{d1}) + a_1^2\cos^2(\beta+\psi_1)\phi^2(x_{d1})} - \delta_1\right) \\
&\quad \times H\left(\sqrt{a_2^2\cos^2(\beta+\psi_2)\phi^2(x_{d1}) + a_1^2\cos^2(\beta+\psi_1)\phi^2(x_{d1})} - \delta_1\right) \\
&\quad \times \frac{a_2\cos(\beta+\psi_2) - a_1\cos(\beta+\psi_1)}{\sqrt{a_2^2\cos^2(\beta+\psi_2) + a_1^2\cos^2(\beta+\psi_1)}}\cdot\phi^2(x_{d1})\cos(\beta+\psi_1)\,d\beta \\
&\quad + \frac{1}{2\pi\Omega M}\int_0^{2\pi} K_{h2}\left(\sqrt{a_2^2\cos^2(\beta+\psi_2)\phi^2(x_{d2}) + a_1^2\cos^2(\beta+\psi_1)\phi^2(x_{d2})} - \delta_2\right) \\
&\quad \times H\left(\sqrt{a_2^2\cos^2(\beta+\psi_2)\phi^2(x_{d2}) + a_1^2\cos^2(\beta+\psi_1)\phi^2(x_{d2})} - \delta_2\right) \\
&\quad \times \frac{a_2\cos(\beta+\psi_2) - a_1\cos(\beta+\psi_1)}{\sqrt{a_2^2\cos^2(\beta+\psi_2) + a_1^2\cos^2(\beta+\psi_1)}}\cdot\phi^2(x_{d2})\cos(\beta+\psi_1)\,d\beta
\end{aligned} \tag{52}
$$

$$
\begin{aligned}
a_2\dot{\psi}_2 = {} & \frac{k_2-\Omega^2}{2\Omega}a_2 + \frac{1}{2}\varepsilon\Lambda_1\Omega\sin(2) + \frac{1}{2}k_1a_1\Omega\sin(\psi_1-\psi_2) \\
& - \frac{3\varepsilon}{8\Omega}a_2^3k_4 - \frac{\varepsilon}{4\Omega}(a_2a_1)^2\mu - \frac{\varepsilon}{8\Omega}(a_2a_1)^2\mu\cos(2\psi_1-2\psi_2) \\
& - \frac{\varepsilon k_3a_1\dot{\Omega}}{2\Omega}\cos(\psi_1-\psi_2) \\
& - \frac{1}{2\pi\Omega M}\int_0^{2\pi} K_{h1}\left(\sqrt{a_2^2\cos^2(\beta+\psi_2)\phi^2(x_{d1}) + a_1^2\cos^2(\beta+\psi_1)\phi^2(x_{d1})} - \delta_1\right) \\
& \times H\left(\sqrt{a_2^2\cos^2(\beta+\psi_2)\phi^2(x_{d1}) + a_1^2\cos^2(\beta+\psi_1)\phi^2(x_{d1})} - \delta_1\right) \\
& \times \frac{a_2\cos(\beta+\psi_2)+\mu a_1\cos(\beta+\psi_1)}{\sqrt{a_2^2\cos^2(\beta+\psi_2)+a_1^2\cos^2(\beta+\psi_1)}}\cdot\phi^2(x_{d1})\cos(\beta+\psi_2)\,d\beta \\
& - \frac{1}{2\pi\Omega M}\int_0^{2\pi} K_{h2}\left(\sqrt{a_2^2\cos^2(\beta+\psi_2)\phi^2(x_{d2}) + a_1^2\cos^2(\beta+\psi_1)\phi^2(x_{d2})} - \delta_2\right) \\
& \times H\left(\sqrt{a_2^2\cos^2(\beta+\psi_2)\phi^2(x_{d2}) + a_1^2\cos^2(\beta+\psi_1)\phi^2(x_{d2})} - \delta_2\right) \\
& \times \frac{a_2\cos(\beta+\psi_2)+\mu a_1\cos(\beta+\psi_1)}{\sqrt{a_2^2\cos^2(\beta+\psi_2)+a_1^2\cos^2(\beta+\psi_1)}}\cdot\phi^2(x_{d2})\cos(\beta+\psi_2)\,d\beta
\end{aligned} \tag{53}
$$

$$
\begin{aligned}
\dot{\Omega} = {} & -\frac{\varepsilon}{2}m_2\left(a_1a_2\cos(\psi_1-\psi_2)\right) - \varepsilon m_2\left[\frac{1}{2}\Omega a_1\dot{a}_2\dot{\psi}_1\sin(\psi_1-\psi_2) + \frac{1}{2}\dot{\Omega}a_2a_1\sin(\psi_1-\psi_2)\right. \\
& \left. - \frac{1}{2}a_2a_1\Omega^2\cos(\psi_1-\psi_2) - \frac{1}{2}a_2a_1\dot{\psi}_2\Omega\cos(\psi_1-\psi_2)\right] \\
& + \varepsilon m_4\left[\frac{1}{2}\dot{a}_2\Omega\sin(\psi_2) + \frac{1}{2}\dot{\Omega}a_2\sin(\psi_2) + \frac{1}{2}\Omega^2a_2\cos(\psi_2)\right. \\
& + \frac{1}{2}a_2\dot{\psi}_2\Omega\cos(\psi_2) - \frac{1}{2}\Omega\dot{a}_1\cos(\psi_1) - \frac{1}{2}a_1\dot{\Omega}\cos(\psi_1) \\
& \left. + \frac{1}{2}\Omega^2a_1\sin(\psi_1) + \frac{1}{2}a_1\dot{\psi}_1\Omega\sin(\psi_1)\right] + \varepsilon e_0\left(E_0-\Omega E_1\right) \\
& - \frac{\mu e_0}{2\pi M}\int_0^{2\pi} K_{h1}\left(\sqrt{a_2^2\cos^2(\beta+\psi_2)\phi^2(x_{d1}) + a_1^2\cos^2(\beta+\psi_1)\phi^2(x_{d1})} - \delta_1\right) \\
& \times H\left(\sqrt{a_2^2\cos^2(\beta+\psi_2)\phi^2(x_{d1}) + a_1^2\cos^2(\beta+\psi_1)\phi^2(x_{d1})} - \delta_1\right) \\
& \times \sqrt{a_2^2\cos^2(\beta+\psi_2)+a_1^2\cos^2(\beta+\psi_1)}\cdot\phi(x_{d1})\,d\beta \\
& - \frac{\mu e_0}{2\pi M}\int_0^{2\pi} K_{h2}\left(\sqrt{a_2^2\cos^2(\beta+\psi_2)\phi^2(x_{d2}) + a_1^2\cos^2(\beta+\psi_1)\phi^2(x_{d2})} - \delta_2\right) \\
& \times H\left(\sqrt{a_2^2\cos^2(\beta+\psi_2)\phi^2(x_{d2}) + a_1^2\cos^2(\beta+\psi_1)\phi^2(x_{d2})} - \delta_2\right) \\
& \times \sqrt{a_2^2\cos^2(\beta+\psi_2)+a_1^2\cos^2(\beta+\psi_1)}\cdot\phi(x_{d2})\,d\beta
\end{aligned} \tag{54}
$$

The system of coupled first-order differential equations, Eqs. (50)–(54), is solved numerically using Runge-Kutta method. At each integration step, the parameter β assumes a specific value determined by the solution process. Through this numerical procedure, the time-dependent solutions for the parameters a_1, a_2, ψ_1, ψ_2, and Ω are obtained. These solutions are then substituted into Eqs. (41)–(44), yielding the complete dynamical response of the system in both vibrational directions. Finally, the system of Eqs. (17)–(19) is solved analytically.

Results and discussion

The results of the numerical simulations are presented to investigate the non-stationary behavior of the rotor-disk-bearing system under various operating conditions, including rub impact, geometric nonlinearity, and non-ideal excitation. All physical and geometrical properties of the rotor system employed in the simulations are provided in Table2. The numerical solution of Eqs. (17)–(19), obtained using the Runge–Kutta method, is compared and validated against the analytical solution derived via the method of averaging. The system response is examined in terms of amplitude, phase angle, angular velocity, energy input, and the influence of flexible-rigid supports stiffness. Variations in system parameters significantly influence the dynamic response and behavior of the rotational system. Figure 6 illustrates the Campbell diagram of the investigated system, which is conventionally employed for critical speed identification.The analysis reveals that increasing the linear stiffness of the bearing elements leads to a corresponding elevation in the system's natural frequencies. In

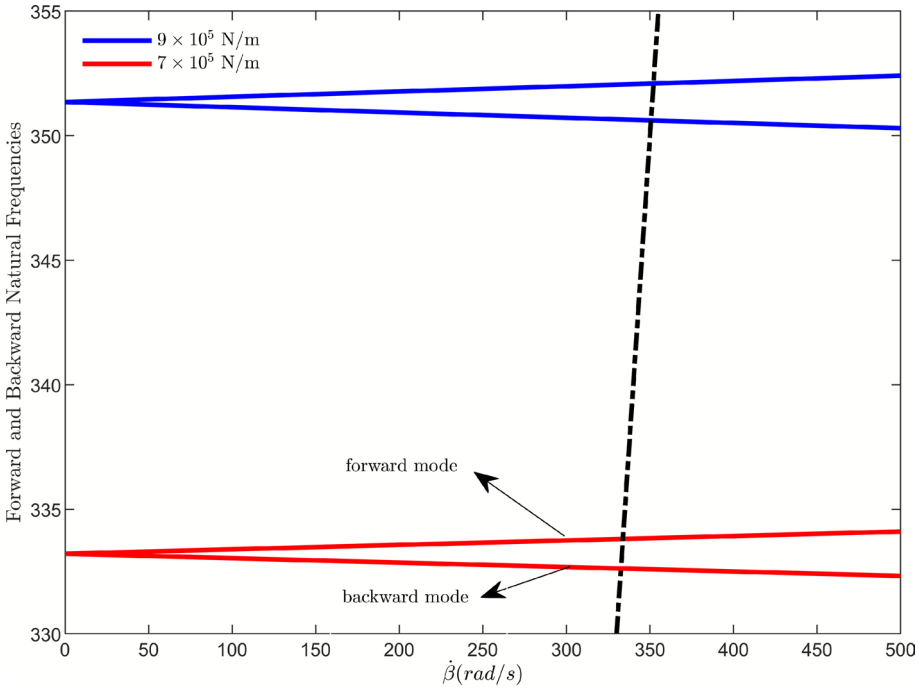

Fig. 6. Campbell diagram for two different values of linear stiffness k_l for the first mode.

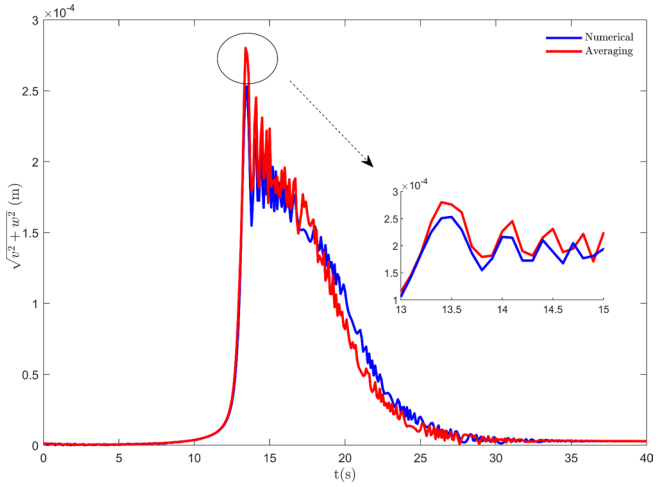

Fig. 7. Amplitude of the rotor during the passage through the first critical speed with considering rub impact.

rotating machinery systems, the natural frequencies demonstrate speed-dependent characteristics, exhibiting a progressive increase with rotational speed for forward mode and decrease for backward mode. Consequently, this stiffness-induced frequency elevation results in a proportional shift in the critical speeds of the system. Figure 7 presents the temporal evolution of the oscillation amplitude $\sqrt{v^2 + w^2}$, comparing the system's dynamic response obtained from both numerical and analytical approaches under rub impact conditions. The results confirm the validity of the proposed solutions, demonstrating exceptional agreement between the analytical solution derived via the averaging method and the numerical integration of the equations of motion. The comparative analysis reveals that the averaging method achieves superior accuracy compared to the multi-scale analytical technique employed in[33] for a simply supported rotor. Notably, the convergence between the analytical and numerical solutions improves with time, with the relative error asymptotically tending to zero. This enhanced predictive capability underscores a key advantage of the averaging method: its ability to accurately model complex dynamical systems while maintaining computational efficiency and robustness.

The time-domain response of the rotor during critical speed traversal is presented in Fig. 8. Characteristic resonant behavior is observed, with substantial vibration amplification leading to periodic rotor-stator collisions between 13–21 s of operation. These impacts generate transient nonlinear forces that significantly alter the

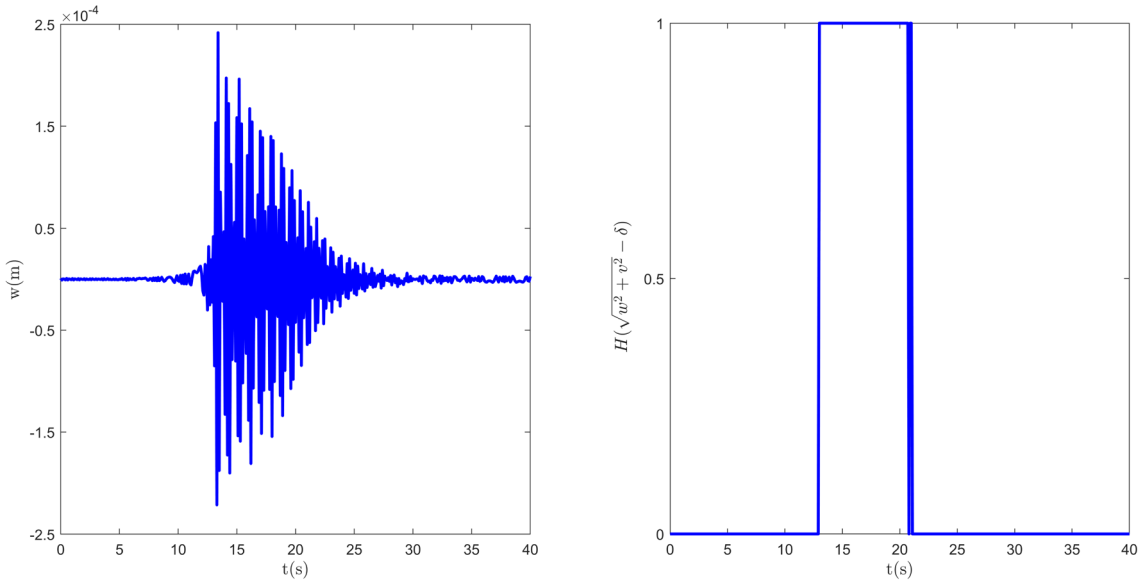

(a) (b)

Fig. 8. (**a**) Time response of the rotor during the passage through the first critical speed, (**b**) occurrence of rub impact.

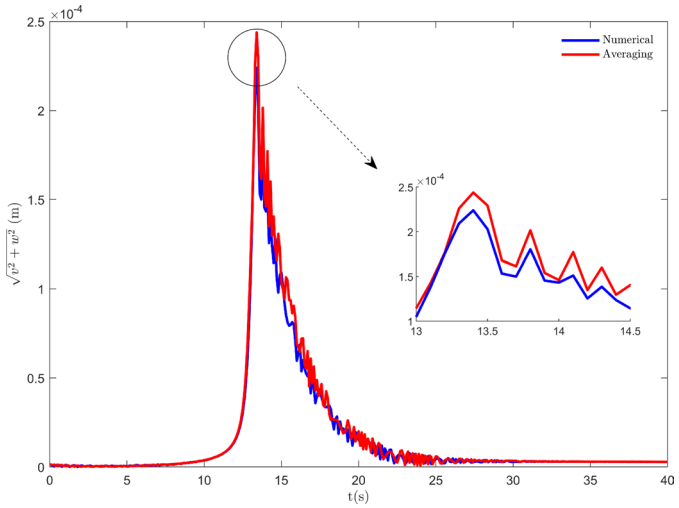

Fig. 9. Amplitude of the shaft during the passage through the first critical speed without considering rub impact.

system dynamics. Post-resonance, as the oscillation amplitude diminishes below the nominal clearance δ (0.3 mm), eliminating the rub effect.

Figure 9 presents a comparative analysis of the system's dynamic behavior under various operating conditions in the absence of rub impact, offering additional insights into the system's dynamic behavior across varying operational parameters. In this scenario, the discrepancy between the two analytical approaches is markedly reduced. This diminished error can be attributed to the elimination of nonlinear effects induced by rub impact, thereby simplifying the system's dynamic response. Conversely, the incorporation of rub impact introduces nonlinear interaction forces between the stator and rotor disk, significantly increasing model complexity and rendering the comparative analysis more intricate. This observation underscores the critical influence of nonlinearities on the accuracy and interpretability of rotor-dynamic simulations.

Figure 10 presents a comparative validation of rotor angular displacement and angular velocity obtained through two distinct methods. Under ideal excitation conditions with constant acceleration, the angular velocity exhibits a linear temporal variation (dashed line), as its time derivative must yield the constant system acceleration. In this figure, the averaging data series represents the results from the analytical averaging method for the rotor's

angular velocity versus time, which have been successfully validated against our numerical solution. The solid reference line with a slope of 1 (a 45-degree line) is not a model output but a conceptual benchmark. It represents the response of an idealized system under a constant torque, which would yield a constant acceleration. The core finding is demonstrated by the clear deviation of the validated numerical and analytical results from this reference line. This divergence proves that the instantaneous derivative (the angular acceleration) of our system's response is not constant but varies with time. Therefore, this line is used specifically to visually underscore that the physical system exhibits **time-varying acceleration** due to non-ideal torque and nonlinear dynamics, rather than the constant acceleration implied by the reference line.

In contrast, non-ideal excitation conditions result in nonlinear angular velocity profiles. The slope of the graph in the non-ideal case decreases with increasing time and rotational velocity (the rotational acceleration). This decrease is consistent with Eq. (20). The angular displacement is also determined through direct numerical computation in one approach, while the analytical method employs numerical integration of the velocity function. Excellent agreement between these independent approaches confirms the validity of both solution methods, demonstrating consistent results despite their different mathematical foundations.

Figure 11 demonstrates a critical behavioral difference in rotor systems based on rub impact conditions. For systems experiencing rotor-stator contact, when the excitation torque falls below the critical threshold of 197 (N m), three distinct phenomena occur: the system fails to traverse the critical speed region, the Sommerfeld effect becomes manifest, and resonance timing characteristics are significantly altered. This contrasts sharply with non-rub systems where the same torque level permits successful critical speed passage.As illustrated in Fig. 12, a reduction in clearance leads to intermittent rotor-stator contact, even at relatively low oscillation amplitudes. This contact introduces strong nonlinear forces into the system dynamics, significantly altering its response. Interestingly, under an applied torque that would typically allow smooth passage through the critical speed, the decreased clearance precipitates the Sommerfeld effect, trapping energy near resonance.In fact, at lower clearances, the intensity of rubbing increases. Consequently, both the normal and tangential rubbing forces become larger. As the tangential rubbing force increases, the resisting torque also rises. Therefore, the Sommerfeld phenomenon is more likely to occur. The figure clearly demonstrates how diminished clearance disrupts the expected crossing of the critical speed, instead causing sustained high-amplitude oscillations. This phenomenon occurs because the nonlinear impact forces modify the system's effective stiffness and damping characteristics, creating a barrier to resonance traversal. Also Fig. 13 indicates the time intervals during which the rub force is applied, for different torque levels.

The rub-impact condition produces characteristic Sommerfeld behavior wherein the angular velocity remains constant while vibration amplitudes exhibit progressive growth, potentially culminating in mechanical failure. This amplitude escalation continues until either the torque increases or system integrity is compromised. The clear divergence in system response between rub and non-rub cases under identical torque conditions (197 N m) provides conclusive evidence that rub impact serves as the primary instigator of the Sommerfeld effect in this configuration.

The analysis reveals that higher excitation torques enable faster critical speed transitions by reducing the system's dwell time in the resonance region.The increased torque input provides sufficient energy to overcome

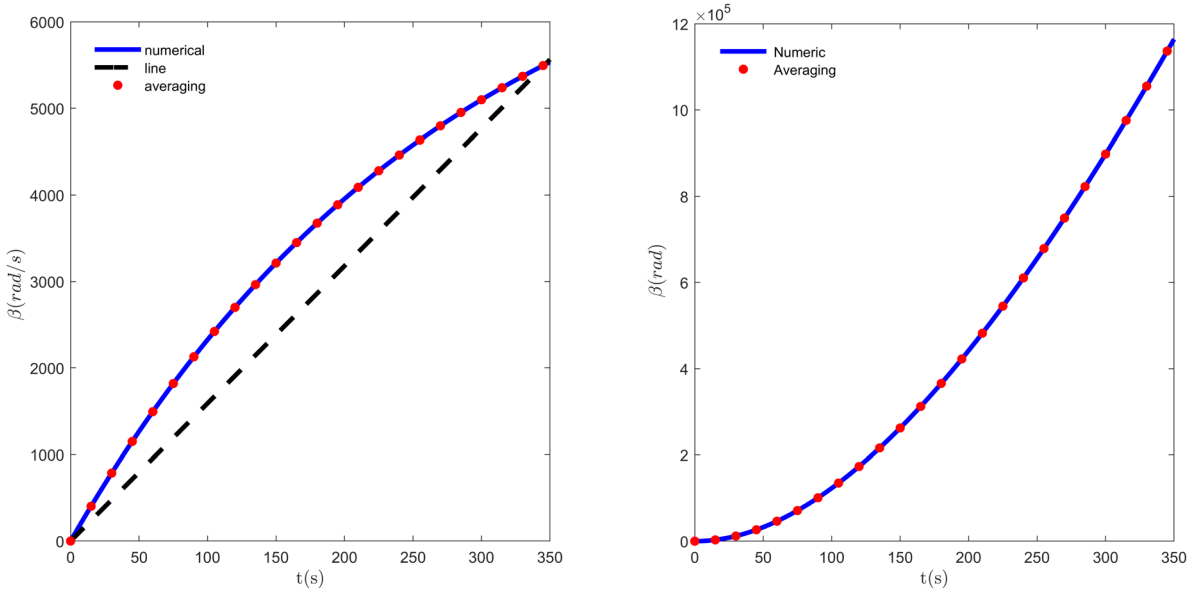

(a) (b)

Fig. 10. (**a**) Variation of the shaft rotational speed without considering rub (**b**) Variation of the shaft angle without considering rub.

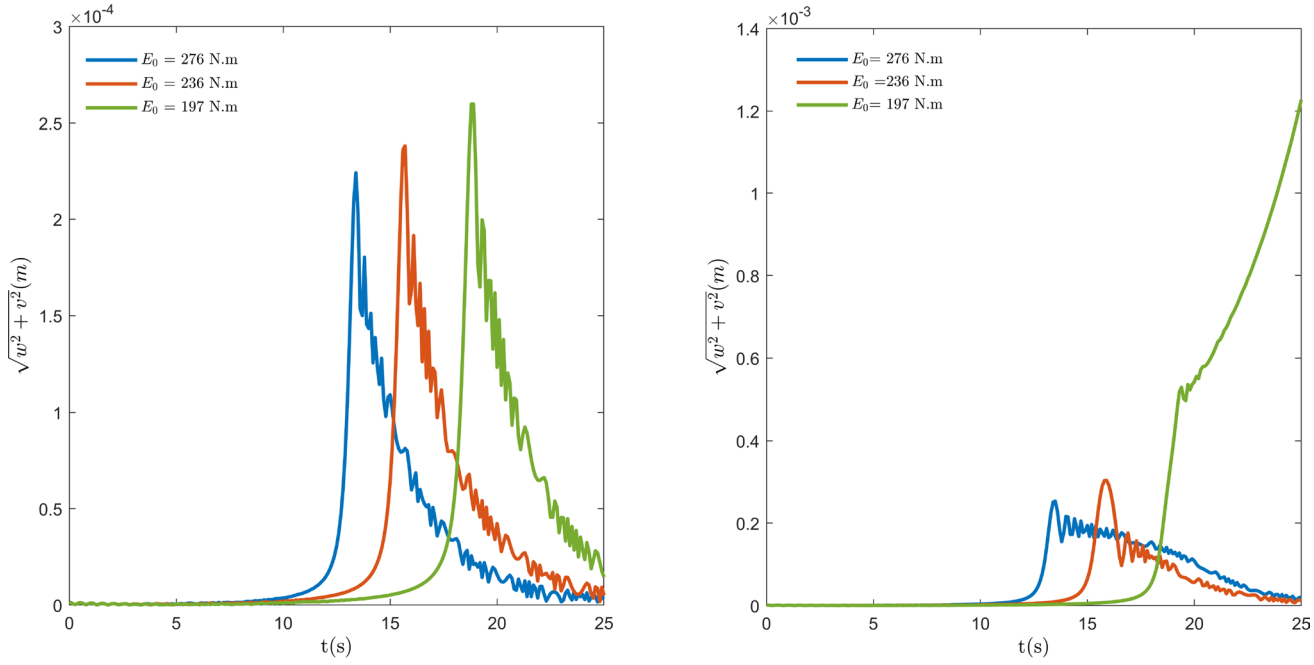

(a) (b)

Fig. 11. Comparison of the rotor vibration amplitude for different values of torque(E_0), (**a**) without considering rub, (**b**) with considering rub.

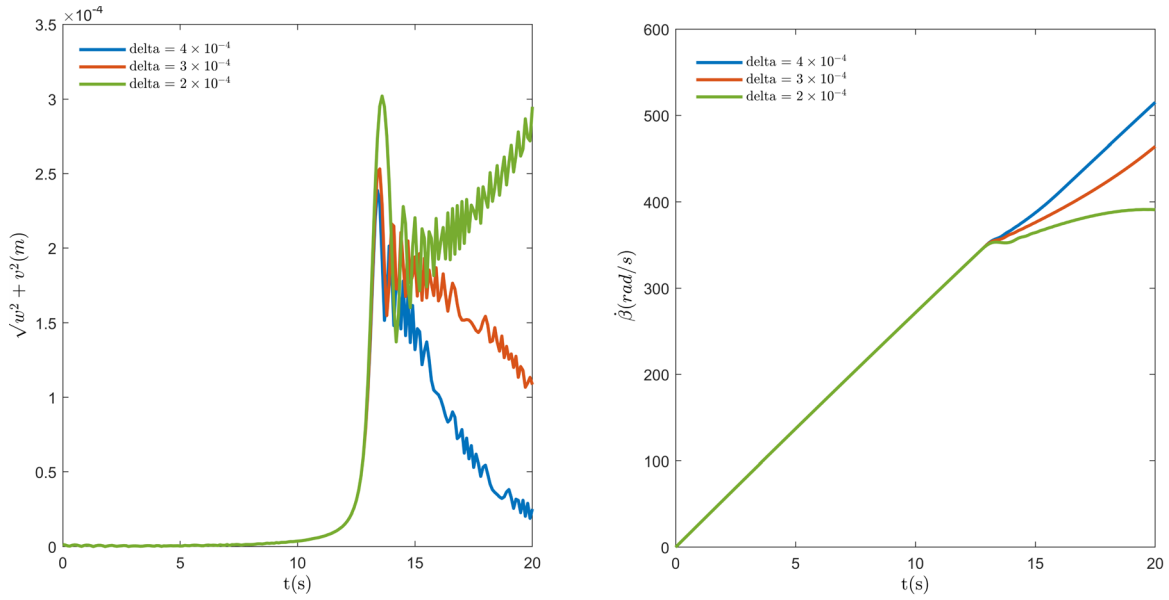

(a) (b)

Fig. 12. Comparison of (**a**) the rotor vibration amplitude, (**b**) rotational speed, under different values of clearance (δ).

the resonance zone more quickly, preventing sustained vibration buildup[32]. In contrast, insufficient torque causes the system to linger near critical speed, where most input energy converts into vibrational energy rather than rotational acceleration. This energy conversion leads to progressively increasing amplitudes while the rotational speed remains nearly constant—the hallmark Sommerfeld effect. The transition from amplitude-dominated to rotation-dominated behavior occurs sharply at the critical torque threshold of 197 N m, below which the system

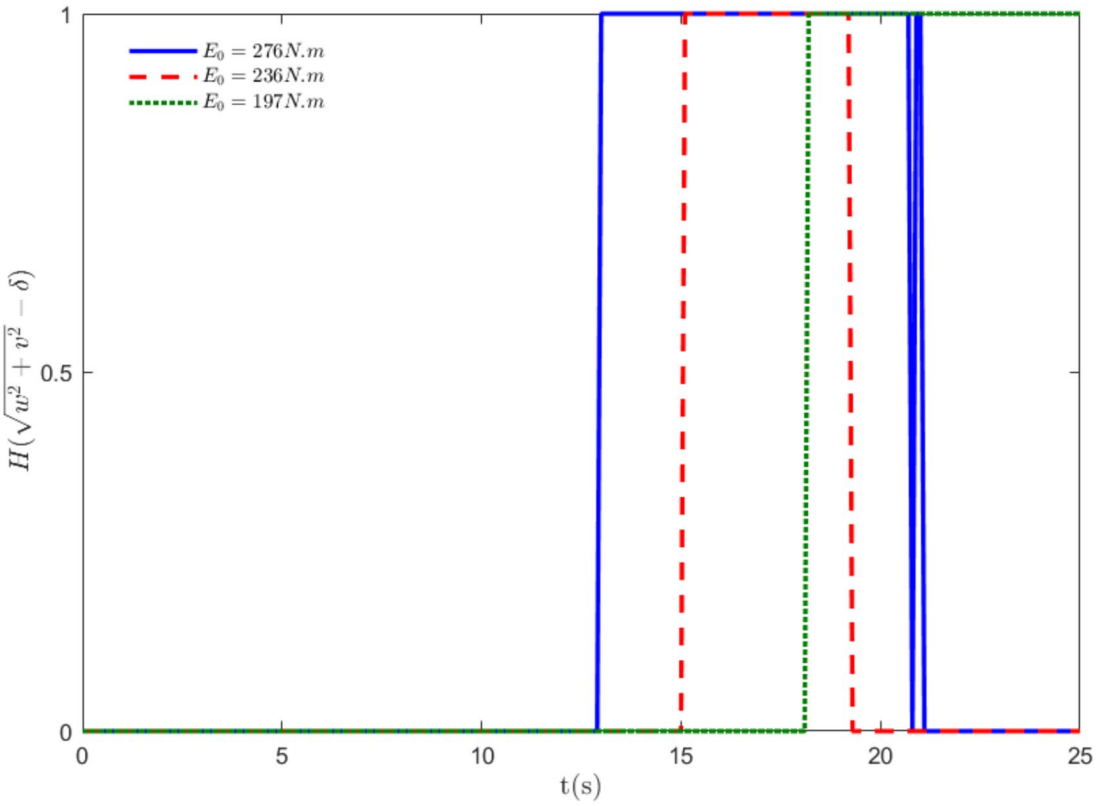

Fig. 13. Occurrence of rub impact for different values of torqe(E_0).

cannot accumulate enough energy to escape resonance trapping. These findings provide fundamental insights into the energy partitioning between rotational and vibrational modes during critical speed passage.

The Sommerfeld effect is influenced by several critical parameters, including rotor damping, nonlinear rotor dynamics, elastic support characteristics, bearing nonlinear stiffness, stator radial stiffness, clearance effects, and unbalance mass distribution. As illustrated in Fig. 14, the system's oscillatory response exhibits significant variation under different damping conditions. At an applied torque of 276 Nm, the system fails to traverse the critical speed regime when the damping coefficient is set to c = 90 Ns/m, resulting in rotational speed stagnation. This phenomenon is attributed to energy entrapment near resonance. However, increasing the damping coefficient facilitates successful resonance passage, even in the presence of rotor-stator rub interactions. Conversely, reduced damping leads to amplified oscillation amplitudes, potentially inducing catastrophic system failure due to excessive vibrational stresses.These findings underscore the pivotal role of damping optimization in mitigating adverse dynamic responses and ensuring stable operation across critical speed thresholds.

The results presented in Figs. 15, 16 and 17 clearly demonstrate the significant impact of rotor-stator rub phenomena on the system's dynamic behavior. In systems experiencing rub, the progressive increase of unbalance masses on the disks and nonlinear stiffness characteristics of the bearings and Radial stiffness of disk prevents the rotor from successfully traversing the first critical speed. In contrast, an equivalent system without rub occurrence can smoothly pass through this critical speed under identical parameter conditions.

Figure 18 highlights the crucial role of flexible bearing modeling in system dynamics, while Fig. 19 provides additional insight by precisely identifying the active periods of rub forces during operation. The results demonstrate that rigid bearing modeling leads to two critical limitations: during rub-active phases, the system fails to pass through critical speeds, and even in rub-free intervals, exhibits delayed resonance response compared to flexible bearing models.

The comparative spectral analysis reveals that the excitation torque serves as a critical bifurcation parameter, steering the rotor system into one of two distinct nonlinear dynamical regimes with profound implications for its vibrational signature and structural integrity. Under a substantially high torque of $276\ \mathrm{N}\cdot\mathrm{m}$, the system rapidly traverses its resonant region and settles into a steady-state response characterized by vigorous rub-impact. This state manifests in the frequency domain (Fig. 20) as a broadband spectrum, with significant energy distributed not only across a primary frequency band of 3–4.5 Hz but also across several of its integer multiples, or harmonics. This harmonic activity is a definitive signature of strong nonlinearity, indicating severe waveform distortion due to contact forces. However, because the substantial input energy is dissipated across this wide array of frequency components, the resulting spectral energy density remains comparatively low, with a maximum value of only 6×10^{-4}. Essentially, the energy is spread thin across many frequencies, creating a complex but relatively low-intensity spectral profile. Conversely, a lower torque of $197\ \mathrm{N}\cdot\mathrm{m}$, induces a qualitatively different behavior. The time-domain response(Fig. 11) exhibits Sommerfeld effect prolonged period of minimal oscillation followed

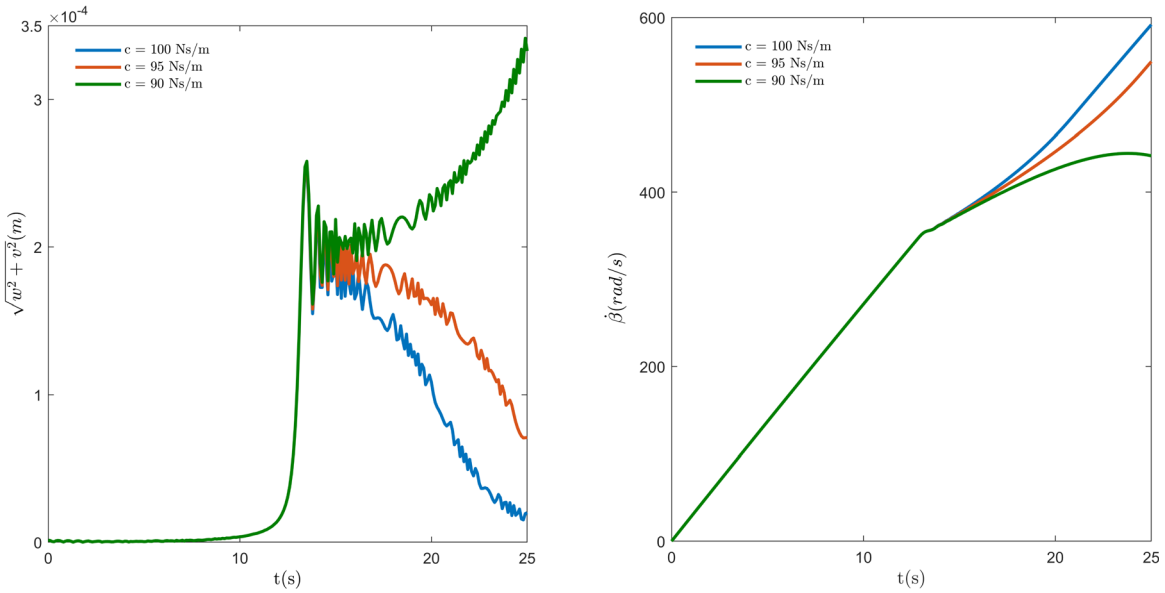

(a) (b)

Fig. 14. Comparison of (**a**) the rotor vibration amplitude, (**b**) rotational speed with different values of damping (C).

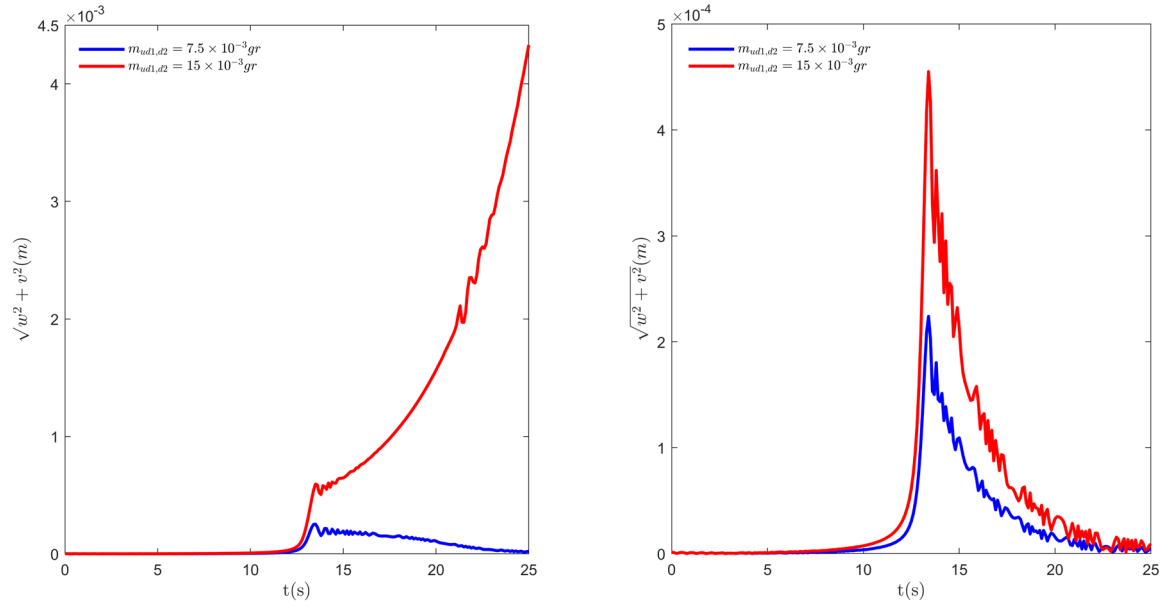

(a) (b)

Fig. 15. Comparison of the rotor vibration amplitude and the probability of the occurrence of the Sommerfeld effect for different values of unbalanced mass (m_{ud}), (**a**) with rub impact, (**b**) without rub impact.

by a sudden, jump like transition to a high-amplitude steady state after approximately 25 seconds. The spectral consequence of this transition, shown in Fig. 21, is striking. Post-jump, the system's vibration collapses into a remarkably simple, narrowband response concentrated at very low frequencies (0.3 Hz), with a complete absence of significant harmonic content. Despite this spectral simplicity and the lower overall energy input, the spectral energy density peaks at a value of 0.025 over forty times greater than that of the high-torque case. This indicates an extreme concentration of the available energy into a single, dominant vibrational mode. The system abandons complexity for focus, trading a broad, dissipative energy distribution for an intense, localized one.

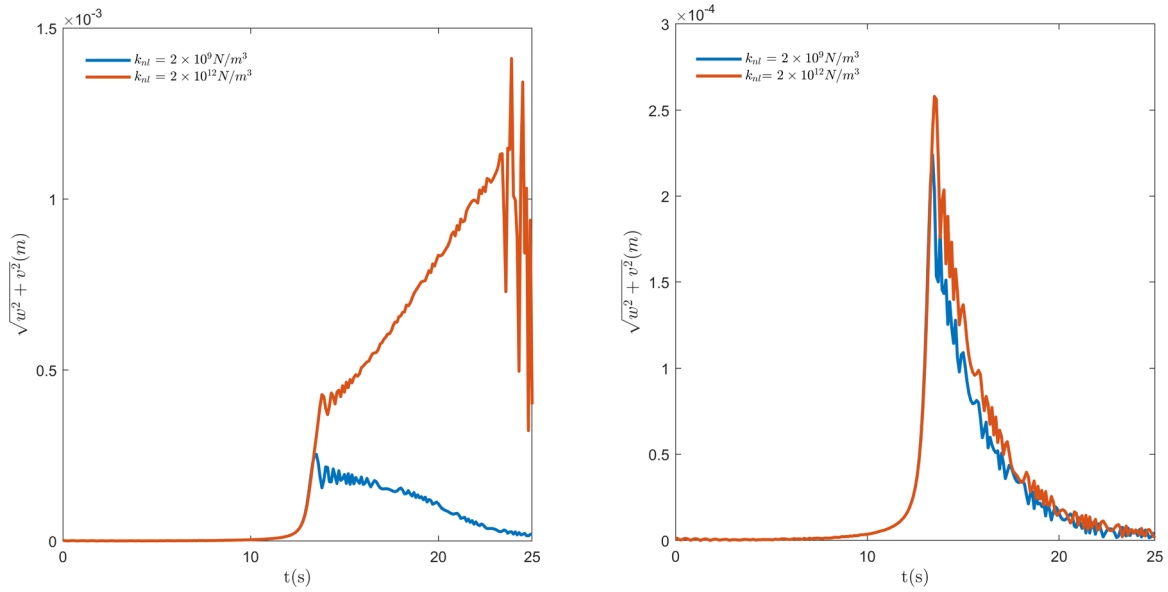

Fig. 16. Comparison of the rotor vibration amplitude and Probability of the occurrence of the Sommerfeld effect for different values of nonlinear stiffness(k_{nl}), (**a**) with rub impact, (**b**) without rub impact.

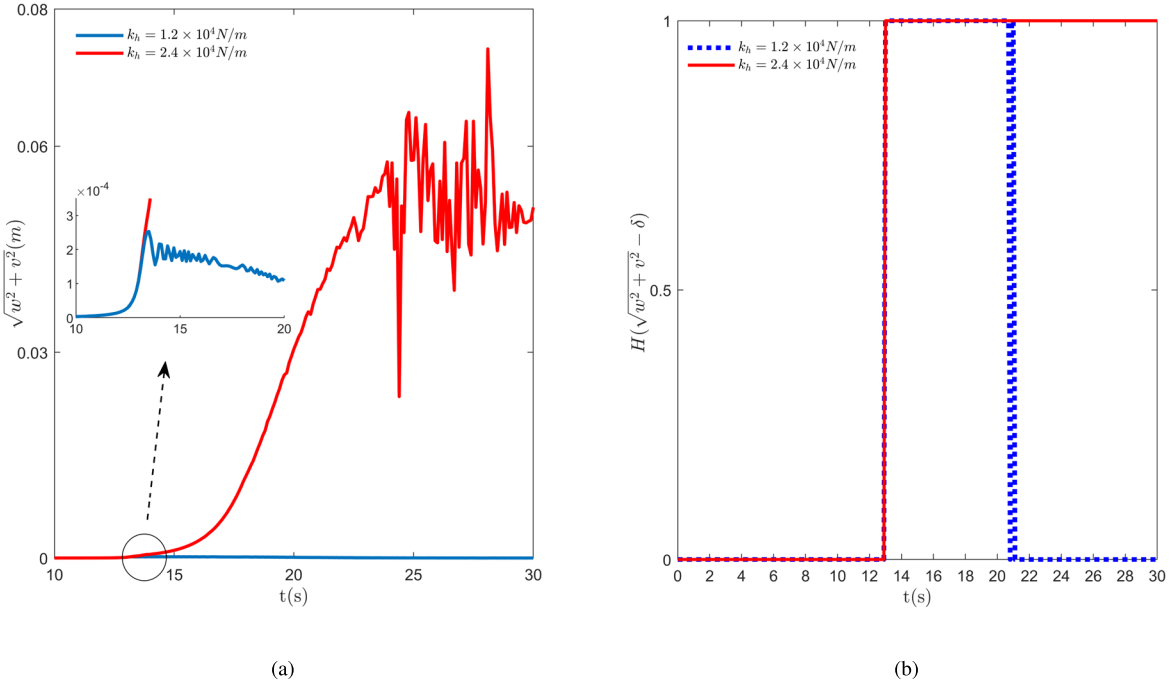

Fig. 17. Comparison of the rotor amplitude and Probability of the occurrence of the Sommerfeld effect for different values of radial stiffness(k_h), (**a**) with rub impact, (**b**) without rub impact.

The torque input fundamentally dictates the nature of the system's vibrational response. A higher torque drives the system into a complex, multi-frequency state. Conversely, a lower, near-threshold torque leads to a spectrally simple but intensely focused response, where energy concentrates into a single low-frequency mode, risking severe localized damage from low-cycle fatigue due to large cyclic strains. Therefore, selecting the operational torque is a strategic decision that chooses the type of dynamic challenge either distributed multi-frequency excitation or concentrated low-frequency stress the structure must endure, which is essential for predictive maintenance and ensuring system longevity.

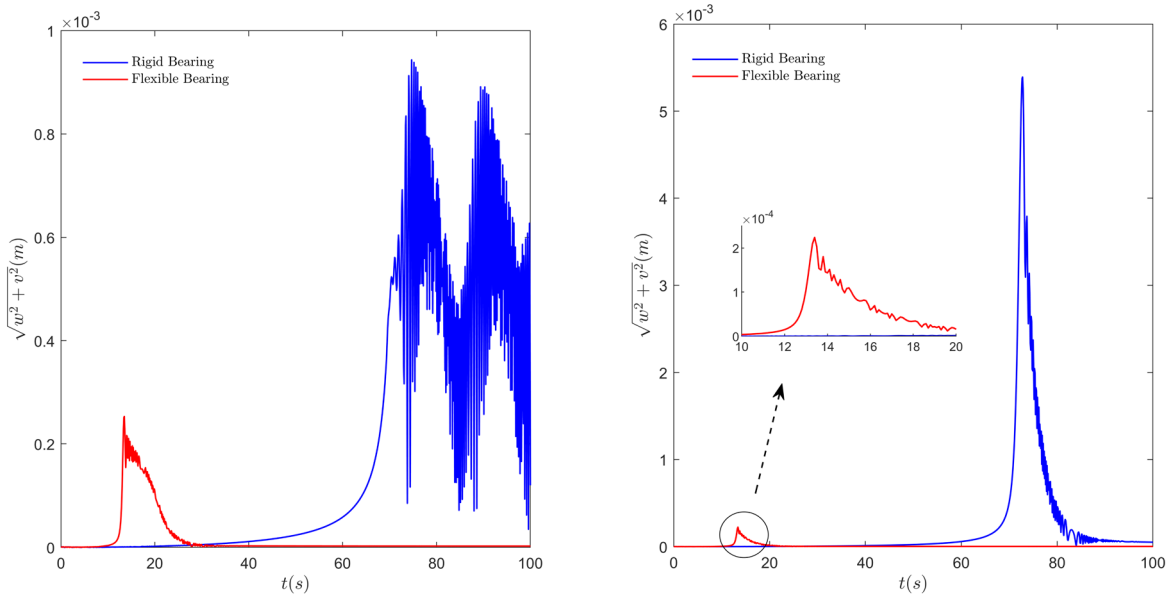

(a) (b)

Fig. 18. Effect of rigid and flexible supports on the amplitude of the rotor, (**a**) with rub impact, (**b**) without rub impact.

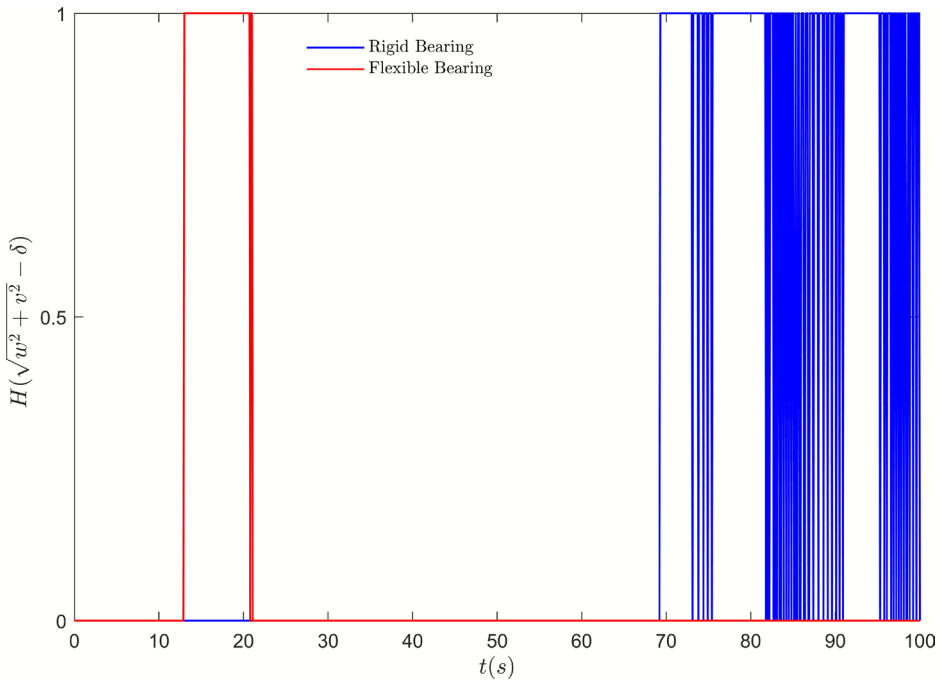

Fig. 19. Occurrence of rub impact for different types of supports.

Conclusion

This research investigates the dynamic modeling of a rotor-disk-bearing system, incorporating nonlinear effects induced by rub-impact, non-ideal excitation, and complex dynamic characteristics including nonlinear foundation stiffness and shaft geometric nonlinearity. Hamilton's principle is employed to derive the equations of motion,the partial differential equations (PDEs) governing the system's dynamics are transformed into ordinary differential equations (ODEs) using the Galerkin method with a single mode approximation. The rub-impact forces were simulated to accurately capture the system's real-world behavior under various operational conditions. Equations are solved using both numerical Runge-Kutta integration and the analytical averaging

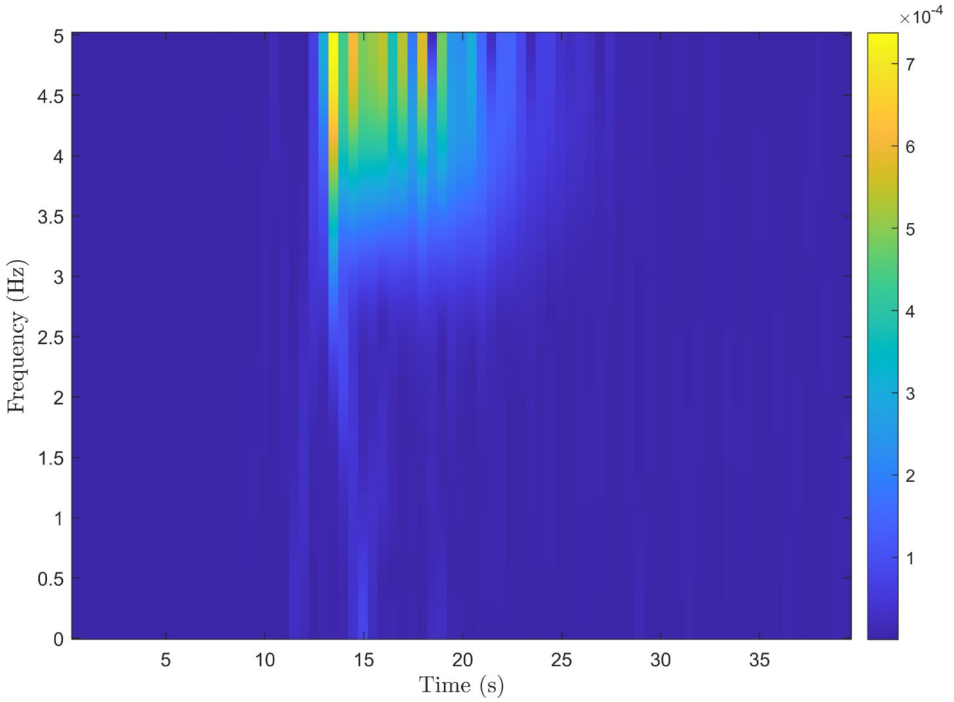

Fig. 20. Frequency spectrum of rotor displacement with considering rub impact($E_0 = 276N.m$).

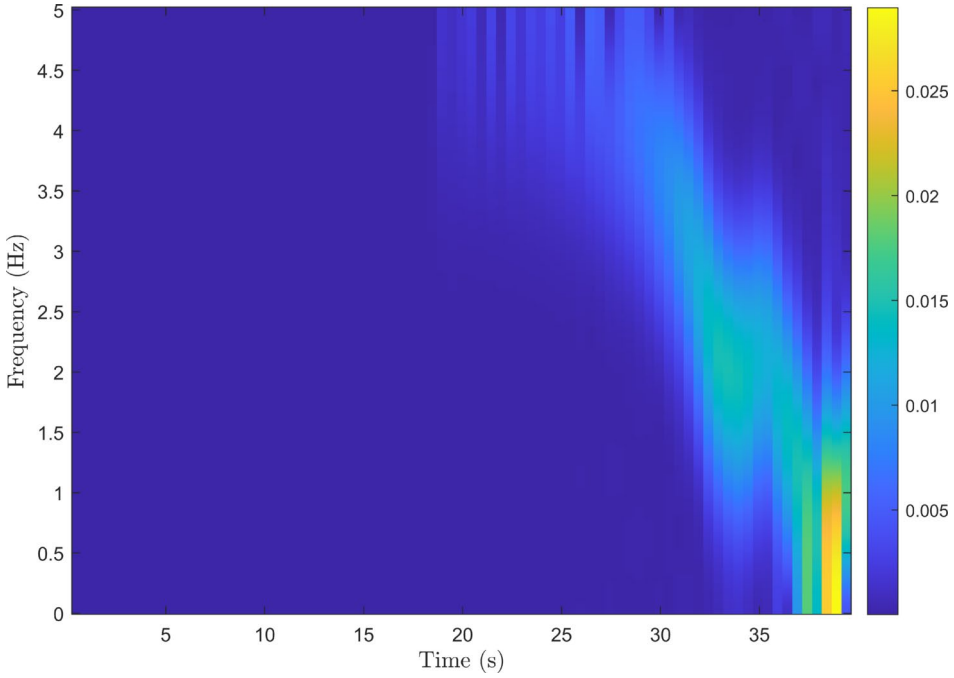

Fig. 21. Frequency spectrum of rotor displacement with considering rub impact($E_0 = 197N.m$).

method. The comparison between these two approaches revealed a minimal error margin, demonstrating the accuracy and consistency of the methods in capturing the system's dynamic response. Numerical simulation results demonstrated that rotor-stator interactions within specific rotational speed ranges can substantially modify the system's dynamic behavior. These alterations are predominantly attributed to forces induced by disk-stator impact, which significantly influence the system's vibrational response. Notably, at critical speeds, these forces were found to trigger sustained resonances and a marked amplification of vibration amplitudes. The analysis further indicated that the system may fail to traverse critical speed, with energy becoming localized

within specific speed regimes. This phenomenon leads to severe oscillatory behavior and the emergence of the Sommerfeld effect.

Furthermore, parametric investigations revealed that key system parameters—including damping coefficient, stator radial stiffness, clearance, applied torque, imbalance mass, and bearing stiffness—exert a pronounced influence on the system's dynamics. A reduction in clearance, damping, and applied torque, coupled with an increase in nonlinear bearing stiffness, stator radial stiffness, and imbalance mass, elevates the propensity for the Sommerefeld effect compared to rub-impact-free systems. Consequently, this intensifies vibrational amplitudes and prolongs residence time in resonant regimes, potentially accelerating system failure.

The study's findings underscore that a comprehensive analysis of rotor-disk-bearing system dynamics necessitates the explicit incorporation of nonlinear effects and non-ideal excitations in modeling frameworks. These insights can facilitate the optimized design of rotating machinery, mitigating unforeseen failures and enhancing operational longevity.

Data availability

The datasets generated during and/or analyzed during the current study are available from the corresponding author on reasonable request.

Appendix

The bending vibration of an Euler-Bernoulli beam with a constant cross-section and in the absence of external forces is governed by the following partial differential equation:

$$c^2 \frac{\partial^4 w}{\partial x^4}(x,t) + \frac{\partial^2 w}{\partial t^2}(x,t) = 0, \quad c = \sqrt{\frac{EI}{\rho A}} \tag{A.1}$$

where E is the Young's modulus, I is the second moment of area, ρ is the mass density, and A is the cross-sectional area. The function $w(x,t)$ represents the transverse (bending) vibration of the beam. Assuming a separable solution of the form:

$$w(x,t) = \phi(x)T(t) \tag{A.2}$$

and substituting it into the governing equation leads to two independent ordinary differential equations:

$$\frac{d^4\phi(x)}{dx^4} - \gamma_i^4 \phi(x) = 0 \tag{A.3}$$

$$\frac{d^2T(t)}{dt^2} + \omega_i^2 T(t) = 0 \tag{A.4}$$

with:

$$\gamma_i^4 = \frac{\rho A \omega_i^2}{EI} \tag{A.5}$$

The general solution for the spatial function $W(x)$ becomes:

$$\phi(x) = c_1 \cos(\gamma_i x) + c_2 \sin(\gamma_i x) + c_3 \cosh(\gamma_i x) + c_4 \sinh(\gamma_i x) \tag{A.6}$$

The constants c_1, c_2, c_3, and c_4 are determined by the boundary conditions at the beam's ends. The beam is elastically supported at both ends, where the applied moment is zero, and the shear force is proportional to the local displacement. These boundary conditions are given by:

$$EI\frac{\partial^3\phi(x)}{\partial x^3}\bigg|_{x=0} = -K_l\phi(0), \quad EI\frac{\partial^2\phi(x)}{\partial x^2}\bigg|_{x=0} = 0 \tag{A.7}$$

$$EI\frac{\partial^3\phi(x)}{\partial x^3}\bigg|_{x=l} = K_l\phi(l), \quad EI\frac{\partial^2\phi(x)}{\partial x^2}\bigg|_{x=l} = 0 \tag{A.8}$$

By substituting the above equations into Eq(A.6), the unknown coefficients are determined, and the function $\phi(x)$ is obtained as:

$$\begin{aligned}\phi(x) =& \frac{\sin(\gamma_i x)\left(\cos(\gamma_i l) - \cosh(\gamma_i l) + \frac{2K_l \sin(\gamma_i l)}{EI\gamma_i^3}\right)}{-\sin(\gamma_i l) + \sinh(\gamma_i l)} + \sinh(\gamma_i x)\left(-\frac{2K_l}{EI\gamma_i^3} + \frac{\cos(\gamma_i l) - \cosh(\gamma_i l) + \frac{2K_l \sinh(\gamma_i l)}{EI\gamma_i^3}}{-\sin(\gamma_i l) + \sinh(\gamma_i l)}\right) \\ &+ \cos(\gamma_i x) + \cosh(\gamma_i x)\end{aligned} \tag{A.9}$$

Received: 7 November 2025; Accepted: 29 January 2026
Published online: 05 February 2026

References

1. Gunter, E. J. Fundamentals of rotor-bearing dynamics using dyrobes: The jeffcott rotor (2016). https://dyrobes.com/wp-content/uploads/2016/04/Fundamentals-of-Rotor-Bearing-Dynamics-Using-Dyrobes-The-Jeffcott-Rotor-E.-J.-Gunter_linked.pdf (accessed 13 Dec 2024).
2. Phadatare, H. P. & Pratiher, B. Nonlinear modeling, dynamics, and chaos in a large deflection model of a rotor-disk-bearing system under geometric eccentricity and mass unbalance. *Acta Mech.* **231**(3), 907–928. https://doi.org/10.1007/s00707-019-02559-9 (2020).
3. Phadatare, H. P. & Pratiher, B. Dynamic stability and bifurcation phenomena of an axially loaded flexible shaft-disk system supported by flexible bearing. *Proc. Inst. Mech. Eng. C J. Mech. Eng. Sci.* **234**(15), 2951–2967. https://doi.org/10.1177/0954406220911957 (2020).
4. Moradi Tiaki, M., Hosseini, S. A. A. & Shaban Ali Nezhad, H. Nonlinear free vibrations analysis of overhung rotors under the influence of gravity. Proc. Inst. Mech. Eng. Part C. J. Mech. Eng. Sci. 234(2), 575–588. https://doi.org/10.1177/0954406219883901 (2020).
5. Nezhad, H. S. A., Hosseini, S. A. A. & Zamanian, M. Flexural-flexural-extensional-torsional vibration analysis of composite spinning shafts with geometrical nonlinearity. *Nonlinear Dyn.* **89**(1), 651–690. https://doi.org/10.1007/s11071-017-3479-0 (2017).
6. Jain, P. H., Bhosle, S. P.: Mathematical modeling, simulation and analysis of non-linear vibrations of a ball bearing due to radial clearance and number of balls. *Mater. Today Proc.* **72**, 927–936. https://doi.org/10.1016/j.matpr.2022.09.093 (2023).
7. Liang, M., Yan, T., Hu, J. & Chen, Z. Effect of rolling bearing parameters on the nonlinear dynamics of offset rotor. *Proc. Inst. Mech. Eng. Part C J. Mech. Eng. Sci.* (2020).
8. Zhou, H. L., Luo, G. H., Chen, G. & Wang, F. Analysis of the nonlinear dynamic response of a rotor supported on ball bearings with floating-ring squeeze film dampers. *Mech. Mach. Theory* **59**, 65–77. https://doi.org/10.1016/j.mechmachtheory.2012.09.002 (2013).
9. Al-Solihat, M. K. & Behdinan, K. Force transmissibility and frequency response of a flexible shaft–disk rotor supported by a nonlinear suspension system. *Int. J. Non-Linear Mech.* **124** (May) (2020). https://doi.org/10.1016/j.ijnonlinmec.2020.103501.
10. Jin, Y., Lu, Z., Yang, R., Hou, L. & Chen, Y. A new nonlinear force model to replace the hertzian contact model in a rigid-rotor ball bearing system. *Appl. Math. Mech. (English Edition)* **39**(3), 365–378. https://doi.org/10.1007/s10483-018-2308-9 (2018).
11. Zhang, H., Lu, K., Zhang, W. & Fu, C. Investigation on dynamic behaviors of rotor system with looseness and nonlinear supporting. *Mech. Syst. Signal Process.* **166** (September 2021), 108400. https://doi.org/10.1016/j.ymssp.2021.108400 (2022).
12. Zhang, X., Han, Q., Peng, Z. & Chu, F. Stability analysis of a rotor-bearing system with time-varying bearing stiffness due to finite number of balls and unbalanced force. *J. Sound Vib.* **332**(25), 6768–6784. https://doi.org/10.1016/j.jsv.2013.08.002 (2013).
13. Bai, C., Zhang, H. & Xu, Q. Subharmonic resonance of a symmetric ball bearing-rotor system. *Int. J. Non-Linear Mech.* **50**, 1–10. https://doi.org/10.1016/j.ijnonlinmec.2012.11.002 (2013).
14. Yang, R., Jin, Y. L., Hou, L. & Chen, Y. S. Super-harmonic resonance characteristic of a rigid-rotor ball bearing system caused by a single local defect in outer raceway. *Sci. China Technol. Sci.* **61**(8), 1184–1196. https://doi.org/10.1007/s11431-017-9155-3 (2018).
15. Wang, P. et al. Nonlinear response of rotor system with bearing dynamic misalignment. *Mech. Based Des. Struct. Mach.* **52**(5), 2532–2553. https://doi.org/10.1080/15397734.2023.2185634 (2024).
16. Zhao, T. Y., Cui, Y. S., Wang, Y. Q. & Pan, H. G. Vibration characteristics of graphene nanoplatelet reinforced disk-shaft rotor with eccentric mass. *Mech. Adv. Mater. Struct.* **29**(24), 3485–3498. https://doi.org/10.1080/15376494.2021.1904525 (2022).
17. Bab, S., Khadem, S. E., Shahgholi, M. & Abbasi, A. Vibration attenuation of a continuous rotor-blisk-journal bearing system employing smooth nonlinear energy sinks. *Mech. Syst. Signal Process.* **84**, 128–157. https://doi.org/10.1016/j.ymssp.2016.06.029 (2017).
18. Cui, Y. & Wang, Y. Effect of disk flexibility on nonlinear vibration characteristics of shaft-disk rotors. *Acta Mech. Sin. Xuebao* **40** (3). https://doi.org/10.1007/s10409-023-23140-x (2024).
19. Zhang, K., Gao, L., Wang, Z., Wang, Z. & Zhang, L. Nonlinear dynamic analysis of ceramic bearing rotor system considering temperature variation fit clearance. *J. Braz. Soc. Mech. Sci. Eng.* **46**(5), 1–15. https://doi.org/10.1007/s40430-024-04838-6 (2024).
20. Zhu, R., Liu, Y., Bojja, N., Qin, Z. & Chu, F. Vibration attenuation of rotating disks via acoustic black holes. *Int. J. Mech. Sci.* **242** (December 2022). https://doi.org/10.1016/j.ijmecsci.2022.108025 (2023).
21. Wang, Y., Cheng, L., Du, J. & Liu, Y. Acoustic black holes in a spinning beam. *J. Vib. Acoust.* **145**(June), 1–27. https://doi.org/10.1115/1.4056791 (2023).
22. Lu, K. et al. Nonlinear dynamic behavior analysis of dual-rotor-bearing systems with looseness and rub-impact faults. *AIAA J.* **61**(11), 5164–5175. https://doi.org/10.2514/1.J062967 (2023).
23. Ouyang, X., Cao, S. & Li, G. *Nonlinear Dynamics of a Dual-Rotor-Bearing System with Active Elastic Support Dry Friction Dampers*, vol. 112 (Springer Netherlands, 2024). https://doi.org/10.1007/s11071-024-09490-2.
24. Phadatare, H. P. & Pratiher, B. Large deflection model for rub-impact analysis in high-speed rotor-bearing system with mass unbalance. *Int. J. Non-Linear Mech.* **132** (February). https://doi.org/10.1016/j.ijnonlinmec.2021.103702 (2021).
25. Amaroju, K., Vijayan, K. & Friswell, M. I. Non-linear modal interactions during rub-impact of a rotating flexible shaft. *J. Vib. Control* **29**(7–8), 1554–1563. https://doi.org/10.1177/10775463211066406 (2023).
26. Bab, S., Khadem, S. E., Abbasi, A. & Shahgholi, M. Dynamic stability and nonlinear vibration analysis of a rotor system with flexible/rigid blades. *Mech. Mach. Theory* **105**, 633–653. https://doi.org/10.1016/j.mechmachtheory.2016.07.026 (2016).
27. Wang, L., Cao, D. Q. & Huang, W. Nonlinear coupled dynamics of flexible blade-rotor-bearing systems. *Tribol. Int.* **43**(4), 759–778. https://doi.org/10.1016/j.triboint.2009.10.016 (2010).
28. Xie, J., Liu, J., Chen, J. & Zi, Y. Blade damage monitoring method based on frequency domain statistical index of shaft's random vibration. *Mech. Mach. Theory* **165** (December 2020). https://doi.org/10.1016/j.ymssp.2021.108351 (2022).
29. Yu, P., Zhang, D., Ma, Y. & Hong, J. Dynamic modeling and vibration characteristics analysis of the aero-engine dual-rotor system with fan blade out. *Mech. Syst. Signal Process.* **106**, 158–175. https://doi.org/10.1016/j.ymssp.2017.12.012 (2018).
30. She, H., Li, C., Tang, Q. & Wen, B. Effects of blade's interconnection on the modal characteristics of a shaft-disk-blade system. *Mech. Syst. Signal Process.* **146**. https://doi.org/10.1016/j.ymssp.2020.106955 (2020).
31. Zeng, J., Zhao, C., Ma, H., Yu, K. & Wen, B. Rubbing dynamic characteristics of the blisk-casing system with elastic supports. *Aerosp. Sci. Technolo.* **95** (2019). https://doi.org/10.1016/j.ast.2019.105481.
32. Mahmoudi, A., Hosseini, S. A. A. & Zamanian, M. Non-stationary analysis of a rotating shaft with geometrical nonlinearity during passage through critical speeds. *Appl. Math. Model.* **46**, 433–449. https://doi.org/10.1016/j.apm.2017.01.078 (2017).
33. Mahmoudi, A., Hosseini, S. A. A. & Zamanian, M. Nonstationary analysis of nonlinear rotating shafts passing through critical speed excited by a nonideal energy source. *Proc. Inst. Mech. Eng. C J. Mech. Eng. Sci.* **232**(4), 572–584. https://doi.org/10.1177/0954406216684364 (2018).
34. Kafi, H. R. & Hosseini, S. A. A. Dynamic analysis of nonlinear rotating composite shafts excited by non-ideal energy source. *ZAMM Zeitschrift fur Angewandte Mathematik und Mechanik* **99**(5), 1–25. https://doi.org/10.1002/zamm.201800279 (2019).
35. Bab, S., Najafi, M., Sola, J. F. & Abbasi, A. Annihilation of non-stationary vibration of a gas turbine rotor system under rub-impact effect using a nonlinear absorber. *Mech. Mach. Theory* **139**, 379–406. https://doi.org/10.1016/j.mechmachtheory.2019.05.005 (2019).
36. Iskakov, Z. & Jamalov, N. Resonant vibrations of a non-ideal gyroscopic rotary system with nonlinear damping and nonlinear stiffness of the elastic support. *MethodsX* **10**, 101993. https://doi.org/10.1016/j.mex.2022.101993 (2023).

37. Rokn-abadi, M. & Amirzadegan, S. Nonlinear modeling of a misaligned rotor under non-stationary operating conditions. *J. Vib. Acoust.* https://doi.org/10.1177/10775463231174269 (2024).
38. Sghaier, E., Bourdon, A., Rémond, D., Dion, J. L. & Peyret, N. Coupled bending torsional vibrations of non-ideal energy source rotors under non-stationary operating conditions. *Int. J. Mech. Sci.* **163**, 105155. https://doi.org/10.1016/j.ijmecsci.2019.105155 (2019).
39. Cveticanin, L., Zukovic, M. & Balthazar, J. M. Dynamics of Mechanical Systems with Non-Ideal Excitation (2018).
40. Harris, T. A. & Kotzalas, M. N. *Essential Concepts of Bearing Technology*, 5th edn (CRC Press, 2007).
41. Fedorov, A. & Fradkov, L. *Dynamics of Mechanical Systems with Non-Ideal Excitation, Vol. 49 of Lecture Notes in Applied and Computational Mechanics* (Springer, 2011). https://doi.org/10.1007/978-3-642-16994-2.

Author contributions
M.A.G.: Conceptualization, methodology, software, formal analysis, investigation, data curation, writing-original draft, visualization. S.B.: Conceptualization, methodology, validation, resources, writing-review and editing, supervision. M.K.M.: Conceptualization, methodology, resources, writing-review and editing, supervision, project administration.

Funding
The author(s) received no financial support for the research, authorship, and publication of this article.

Declarations

Competing interest
The authors declare no competing interests.

Additional information
Correspondence and requests for materials should be addressed to M.K.M.

Reprints and permissions information is available at www.nature.com/reprints.

Publisher's note Springer Nature remains neutral with regard to jurisdictional claims in published maps and institutional affiliations.